

SceneLCM: End-to-End Layout-Guided Interactive Indoor Scene Generation with Latent Consistency Model

Yangkai Lin

School of Electronic and Information Engineering
South China University of Technology
202210182091@mail.scut.edu.cn

Jiabao Lei

School of Data Science
The Chinese University of Hong Kong,
Shenzhen
jiabaolei@link.cuhk.edu.cn

Kui Jia*

School of Data Science
The Chinese University of Hong Kong,
Shenzhen
kuijia@cuhk.edu.cn

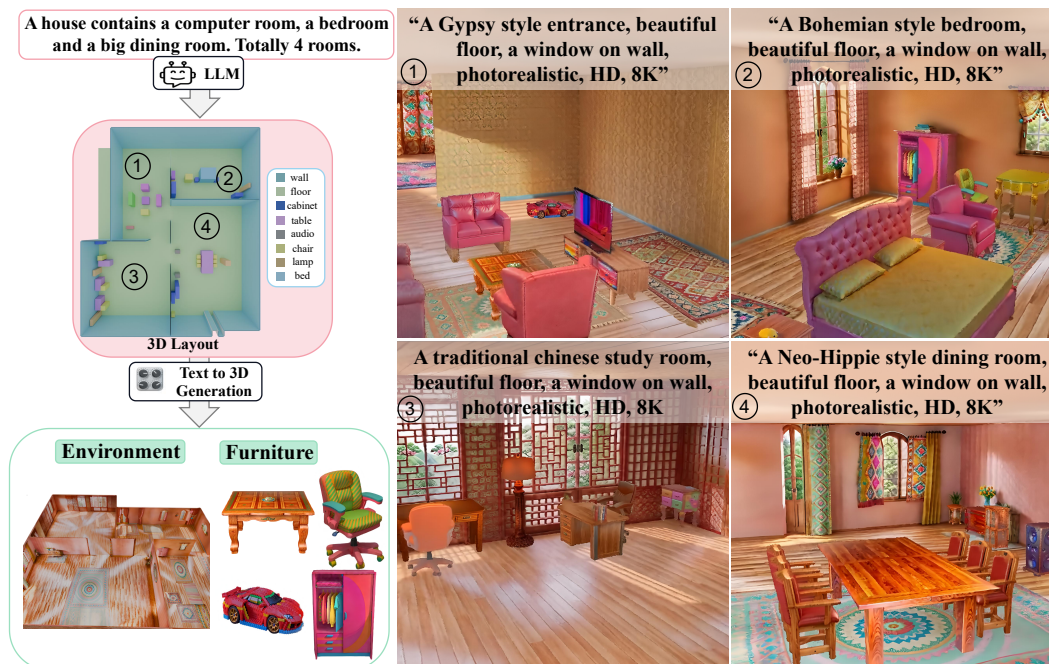


Figure 1: Given a textual description of the house, our end-to-end framework enables automated generation of multi-room, multi-scale indoor scene, while supporting controllable scene generation, physically editing, and texture editing of environment.

Abstract

Our project page: <https://scutyklin.github.io/SceneLCM/>. Automated generation of complex, interactive indoor scenes tailored to user prompt remains a formidable challenge. While existing methods achieve indoor scene synthesis, they struggle with rigid editing constraints, physical incoherence, excessive hu-

*Corresponding author.

man effort, single-room limitations, and suboptimal material quality. To address these limitations, we propose SceneLCM, an end-to-end framework that synergizes Large Language Model (LLM) for layout design with Latent Consistency Model(LCM) for scene optimization. Our approach decomposes scene generation into four modular pipelines: (1) Layout Generation. We employ LLM-guided 3D spatial reasoning to convert textual descriptions into parametric blueprints(3D layout). And an iterative programmatic validation mechanism iteratively refines layout parameters through LLM-mediated dialogue loops; (2) Furniture Generation. SceneLCM employs Consistency Trajectory Sampling(CTS), a consistency distillation sampling loss guided by LCM, to form fast, semantically rich, and high-quality representations. We also offer two theoretical justification to demonstrate that our CTS loss is equivalent to consistency loss and its distillation error is bounded by the truncation error of the Euler solver; (3) Environment Optimization. We use a multiresolution texture field to encode the appearance of the scene, and optimize via CTS loss. To maintain cross-geometric texture coherence, we introduce a normal-aware cross-attention decoder to predict RGB by cross-attending to the anchors locations in geometrically heterogeneous instance. (4)Physically Editing. SceneLCM supports physically editing by integrating physical simulation, achieved persistent physical realism. Extensive experiments validate SceneLCM’s superiority over state-of-the-art techniques, showing its wide-ranging potential for diverse applications.

1 Introduction

While generating diverse indoor scenes is critical for Embodied AI and AR/VR, creating multi-room environments with persistent physical realism remains challenging due to high knowledge requirements and computational costsCommunity [2018], Unity Technologies [2023], Epic Games. Recent studies have attempted to tackle this problem by developing generative models for scene creation via various approaches, including text-to-3d methodsYang et al. [2024a], Liang et al. [2024], Zhong et al. [2024], Li et al. [2024a,b] and Layout-based Object retrievalYang et al. [2024b], Fu et al. [2024], Wang et al. [2024b], Lin and Mu [2024].

Despite these recent efforts, generating diverse, realistic, interactive multi-room environments due to the inherent drawbacks and assumptions made in the pipeline. Contemporary text-to-3D generation frameworks, while advancing high-fidelity asset generation with photorealistic texture details, face systemic challenges in four critical dimensions: (1) Fail to generate multi-room environments; (2) Inability to decouple furniture components, restricting parametric editing and physical plausibility;(3) Long completion time in large-scale environment; (4) Lack of end-to-end pipeline automation, requiring 3D artists to manually define layouts and camera trajectoryYang et al. [2024a], Li et al. [2024a]. In contrast, Layout-based Object retrieval demonstrate superior scalability and flexible in synthesizing large-scale scene; they also presents its own limitations, (1) Single-step inference paradigms of LLMBrown et al. [2020], Achiam et al. [2023], Guo et al. [2025] often lead to position overlap and orientation inaccuracies; (2) Failing generate texture-rich environments while lacking critical compositional elements (window, ceiling, wall). (3) Necessity of extensive database preparation for inference.

To this end, we propose SceneLCM, an End-to-End generative framework that synergistically integrates text-to-3D and Layout-based generation methods, systematically addressing all aforementioned challenges. We first formulate indoor scene generation pipeline as four modular subtasks: layout generation, furniture generation, environment generation, and physical edition. Specifically, given a text description, we translate it into 3D layout following previous workFu et al. [2024] as shown in Figure 1. To mitigate void regions and misoriented placement, we propose an iterative programmatic verification mechanism that converts layout parameters into executable programs, followed by LLM-driven iterative refinement cycles where the program undergoes continuous modification and execution until an error-free condition is achieved. Next, we propose Consistency Trajectory Sampling loss(CTS) for furniture generation, which leverage latent consistency modelLuo et al. [2023] to maintain the consistency condition along the PF-ODE trajectory. In detail, the CTS loss is primarily structured around conducting matching between two interval steps in the ODE trajectory. Furthermore, we observe that substituting noise image with rendered image significantly enhances training efficiency while preserving fine-grained texture details. Furthermore, we provide an in-depth

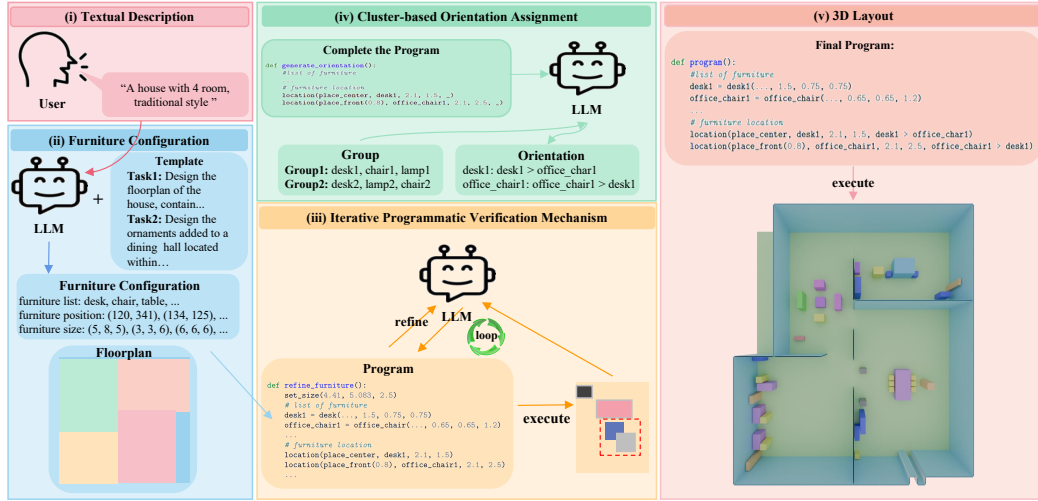


Figure 2: The overview of Layout Generation. Taking a free-form textual input, our pipeline generates the 3D layout by: (i)(ii)comprehending and elaborating on the textual prompt through querying an LLM with templated prompts; (iii)transfer the floorplan and furniture configuration into program and apply Iterative Programmatic Verification Mechanism refine the program to achieve the overlap error-free condition; (iv) Organize furniture into groups and generate direction for each group through completing the program; (v)convert the final program into 3D layout.

theoretical analysis and reveal that the CTS loss and consistency loss Song et al. [2023] exhibit an explicit mathematical relationship.

Following the acquisition of finalized furniture assets, we place them into the 3D layout and subsequently optimize the texture of the environment. Prior approaches iteratively inpaint the texture map frame by frame Huang et al. [2024b], Wang et al. [2024a], however, this approach results in texture synthesis strictly governed by underlying geometry, and our 3D layout comprising discrete planar meshes invalidates texture inpaint methods. At its core, following SenceTex Chen et al. [2024a], we employ a multi-resolution texture field to implicitly represent the texture of the layout. To secure the style consistency and enhance the texture details, we incorporate normal-aware cross-attention decoder and decode RGB values via cross-attending to the pre-sampled anchors scattered across each instance which belongs to the same normal. We further apply CTS loss for texture optimization. Moreover, to enable adaptive multi-scale environment optimization, we propose a zigzag adaptive camera trajectory and several techniques that ensure complete and high-quality texture generation.

We present the first controllable end-to-end multi-room indoor scene generation framework with physically plausible editing support. We show that SceneLCM has the capacity to generate complex scenes that support fully interactable and physical plausible editing. Experimental results demonstrate that our approach generates objects and environments with more details and higher fidelity than SOTA.

2 Related Works

Differentiable 3D Representation The differentiable nature of neural rendering paradigms such as NeRF Mildenhall et al. [2021], SDF Park et al. [2019], and Gaussian Splatting Kerbl et al. [2023] establishes a unified framework for 3D representation learning, geometric manipulation, and photorealistic rendering. This intrinsic compatibility with gradient-based optimization algorithms enables continuous refinement of volumetric scene parameters through backpropagation, establishing a closed-loop pipeline where loss-driven parameter updates progressively enhance scene fidelity. Particularly, the recent approach Kerbl et al. [2023] and its variants Huang et al. [2024a], Yu et al. [2024], Lu et al. [2024], Guédon and Lepetit [2024] modeling 3D scenes with 3D Gaussians have achieved superior real-time rendering via rasterizer. Unlike implicit representations Mildenhall et al. [2021], Park et al. [2019], 3D Gaussians provide more flexible framework, simplifying the integration of multiple scenes. Therefore, we adopt 3D Gaussians for their explicit representation and ease of scene combination.

Text-to-3D Generation One work can be categorized as Large Generative Model(LGM)Ren et al. [2024], Vahdat et al. [2022], Wu et al. [2024a], Zhang et al. [2023, 2024c], Xiang et al. [2024]. Early LGM leverage generative modelsHo et al. [2020], Goodfellow et al. [2014] for various representationsLuo and Hu [2021], Hui et al. [2022], Chen et al. [2023a]. To enhance both quality and efficiency, recent studiesZhang et al. [2024c], Xiang et al. [2024], Zhao et al. [2023] have resorted to generation in a more compact latent space. However, these methods often yield lacking of texture detail(e.g., hair strands) and unrealistic appearance.

Another line of work can be categorized as text-to-3D generationLi et al. [2024b], Poole et al. [2022], Wu et al. [2024b], Yan et al. [2025], Li et al. [2024a], Zhong et al. [2024], Liang et al. [2024], Chen et al. [2024b]. As a pioneer, the score distillation sampling (SDS) paradigm for distilling 2D text-to-image diffusion models is proposed in DreamFusionPoole et al. [2022] and SJCWang et al. [2023a]. During the distillation process, the learnable 3D representation with rendering is optimized by the gradient to make the rendered view match the given text. Many recent works follow the SDS paradigm and studied for various aspectsHuang et al., Zhu et al., Lin et al. [2023], Wang et al. [2023b], Chen et al. [2023b], Liang et al. [2024]. Some worksWu et al. [2024b], Li et al. [2024b], Zhong et al. [2024], Chen et al. [2024b] integrating consistency modelsSong et al. [2023] exhibit substantial relevance to ours. However, existing approaches merely derive conceptual inspiration from consistency modelSong et al. [2023], achieving structural analogy without explicitly formalizing the mathematical linkage between consistency function and their methodsWu et al. [2024b], Li et al. [2024b], Zhong et al. [2024], Chen et al. [2024b]. In contrast, we conduct an in-depth analysis of consistency model and mathematically formulate the intrinsic relationship between our CTS loss and consistency loss.

Indoor Scene Generation The Indoor Scene Generation tasks can be categorized into Layout-based Objects retrieval and text-to-3D Generation. The first methods mainly focus on layout generation and then retrieve objects from database according to layout. In the early stage, some worksLin and Mu [2024], Zhai et al. [2024] train generative modelsGoodfellow et al. [2014], Ho et al. [2020] to generate layout. However, the 3D scene datasets are considerable small compared with object datasets. Thus models trained on these datasets are less robust and lack of novelty. Recently, some worksFu et al. [2024], Yang et al. [2024b], Deng et al. [2025] utilize the LLM/VLMBrown et al. [2020], Achiam et al. [2023] to analysis user text prompts and use CLIP to retrieve relevant objects. Though these methods generate editable scenes, they often neglect texture optimization, require annotated database, and omit key scene elements (e.g., window, ceiling, wall). Text-to-3D scene generation methods face significant limitations. Zhang et al. [2024b], Höllein et al. [2023], Schult et al. [2024] replying on inpainted images for scene completion can generate realistic visuals but suffer from limited 3D consistency. Moreover, such methods typically do not allow for the editing of furniture. While some methodsLi et al. [2024a], Yang et al. [2024a], akin to ours, attempt to merge layout to enhance controllability, and sdsPoole et al. [2022] loss for realistic scene. However, they are incapable of autonomously generating layouts and can accommodate only a limited number of objects. Moreover, They cannot perform physically plausible editing. Our method addresses all the aforementioned issues and proposes an end-to-end, controllable, high-detail generative framework that supports physically plausible editing.

3 Preliminary

Consistency Model(CM)Song et al. [2023], Luo et al. [2023] is proposed to facilitate a single-step or low number of function evaluations (NFEs) generation by distilling knowledge from pre-trained DMHo et al. [2020]. It defines a consistent function $f_\theta(\cdot; \cdot)$ with trainable parameters θ that directly predicts the denoised image x_0 given t and x_t . And $f_\theta(\cdot; \cdot)$ is trained by minimizing self-consistency distillation loss defined as:

$$L_{CD}(\theta, \theta^-) = \mathbb{E}[w(t) \| f_\theta(x_{t_{n+1}; t_{n+1}}) - f_{\theta^-}(\hat{x}_{t_{n+1} \rightarrow t_n}; t_n) \|_2^2], \quad (1)$$

where $0 = t_1 < t_2 \dots < t_N = T$, $\hat{x}_{t_{n+1} \rightarrow t_n}; t_n$ is calculated given ODE solver $\Phi(\cdot)$. θ^- is updated during training process through an exponential moving average(EMA) strategy. The ultimate goal of CM is to maintain the self-consistency condition along the trajectory $\{x_t\}_{t \in [0, T]}$, satisfying:

$$f(x_t; t) = f(x_{t'}; t') \quad \forall t, t' \in [0, T], \quad (2)$$

Specifically, consistent function f parameterized by the noise prediction model ϵ_θ , as follows:

$$f(x_t, t) = c_{skip}(t)x_t + c_{out}(t)\left(\frac{x_t - \sigma_t \epsilon_\theta(x_t, t)}{\alpha_t}\right), \quad (3)$$

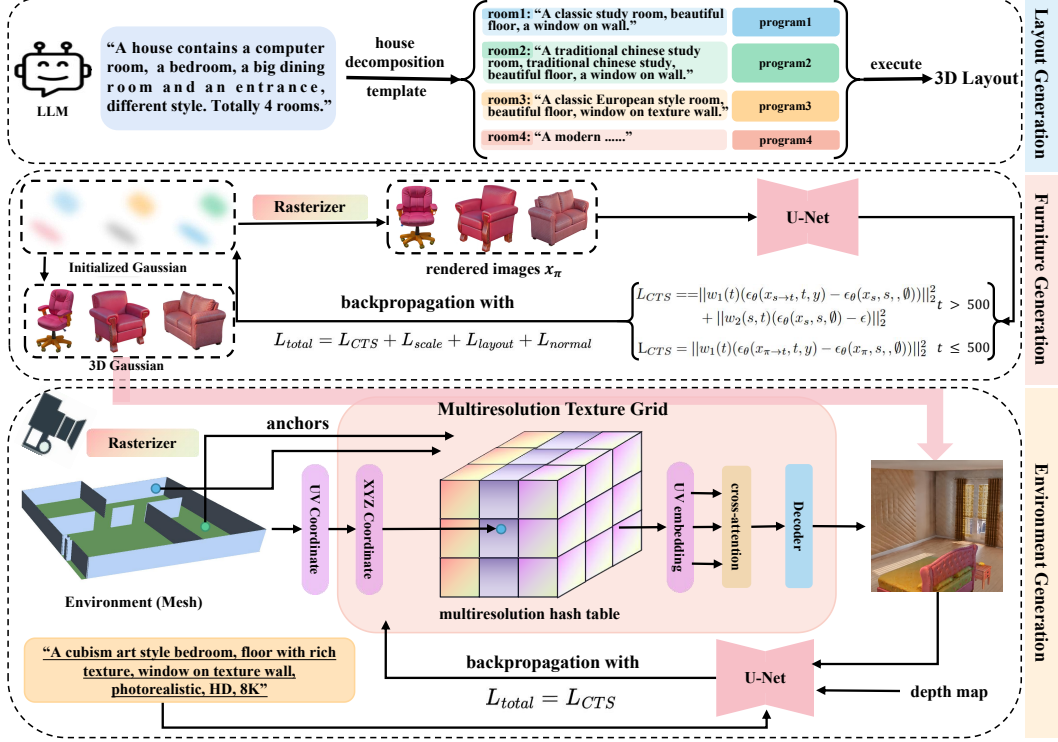


Figure 3: The overview of SceneLCM. We primarily employ CTS loss to jointly generate high-quality furniture and optimize environment appearance. Additionally, SceneLCM ensures scene-wide consistency through camera sampling and allows for flexible editing by integrating furniture with the environments in the scene.

Inspired by CMSong et al. [2023], we propose Consistent Trajectory Sampling to guide the rendered images x_π to match the origin of PF-ODE trajectory.

3D Layout 3D layout acts as a rough outline for the house layout and is defined by semantic bounding boxes which represent layout geometry using mesh. Specifically, we define a house M_e as a set of semantic bounding boxes $B = (p, s, c, n)$, where $p \in \mathbb{R}^3$ is the box center, $s \in \mathbb{R}^3$ is the box size, c the semantic class id, and n the unique name associated with each box. As shown in figure. 2, 3D layout is solely composed of planar components with limited geometric complexity.

Hybrid Rendering Scene layouts combine low-complexity geometry with high-frequency texture and we represent layout geometry using mesh and texture through multiresolution texture field, while parameterizing furniture via 3D Gaussians. We employ a differential rasterizer (i.e., pytorch3dRavi et al. [2020]) to render rgb image I_l and depth map D_l from layout mesh, and Gaussian splatting renderKerbl et al. [2023] to render rgb image I_f and depth map D_f from furniture. The renderings of the scene are obtained by fusing the renderings of furniture and layout, as follows:

$$R = \begin{cases} R_f & \text{if } D_f \leq D_l \\ R_l & \text{if } D_f \geq D_l \end{cases} \quad (4)$$

where R denotes the final RGB image I , R_l is the pixel value from I_l and R_f is from I_f respectively.

4 Method

SceneLCM formulates the indoor scene generation pipeline as four modules: Layout Generation, Object Generation, Environment Optimization, and Physical Editing. First, we modulate the textual input using LLM Achiam et al. [2023] as detailed in Sec. 4.1, which involves user input comprehension and some methodologies for fine-grained layout parameter refinement. Second, in Sec. 4.2, we rapidly create high-fidelity furniture using CTS loss by incorporating LCMLuo et al. [2023], accompanied by two theoretical justification. Third, Sec. 4.3 describes texture field and optimization. Finally, we show that our generated indoor scene can support physical plausible editing, texture editing in Sec. 5.1.

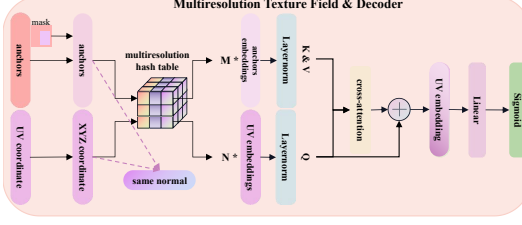


Figure 4: Normal-aware Texture Decoder. We mask out the anchors which have the same normal as the UV coordinate and extract the texture embedding for the XYZ and anchors. Then we employ a cross-attention to produce the final UV embeddings.

Table 1: Quantitative Results of SceneLCM compared with baselines

Methods	Editing	Physics	Multi-room	Time (h)	User Study
Text2Room Höllein et al. [2023]				9.1	4.1
Set-the-Scene Cohen-Bar et al. [2023]	✓			1.6	3.2
DreamScene Li et al. [2024a]	✓			1.2	7
SceneCraft Yang et al. [2024a]			✓	4.5	4.4
Ours	✓	✓	✓	1.2	8.4

4.1 Layout Generation

This initial component of our framework performs four key functions as shown in Figure 2. First, user offer a description of the house to guide and control the generation. Second, it utilizes the LLMs Brown et al. [2020], Achiam et al. [2023], Guo et al. [2025], Liu et al. [2024] to convert the provided input into a 3D layout encompassing house floorplan and furniture configurations Fu et al. [2024]. However, the layouts generated by this simplistic approach suffer from blank area, position overlap and orientation inaccuracies. Third, we propose an iterative programmatic verification mechanism that convert the 3D layout into programs and execute it to check for conflicts. Then we iteratively feed the error and program into the LLM for parameter refinement, cycling this process until error-free conditions are achieved. Moreover, we propose a cluster-based orientation assignment strategy, where scene objects are partitioned into functional groups. Within each group, object orientations are determined not by cardinal directions (e.g., north/south), but through inter-object spatial relations (e.g., chair \rightarrow desk). LLMs can efficiently infer object orientations with minimal local context. Further details and algorithm on these prompts can be found in the Supplementary Material.

4.2 Furniture Generation

Consistency Trajectory Sampling Loss

Consistent3D Wu et al. [2024b] argues that the key to generating a satisfactory 3D model is to accurately perform the 3D ODE sampling using diffusion model. Motivated by this assumption, recent works Li et al. [2024b], Zhong et al. [2024], Chen et al. [2024b] attempt to improve the model’s performance in view of CMSong et al. [2023]. However, these models only adopt the idea of consistency model, but fail to conduct in-depth research on their interrelationships.

Similar to eq. 1, our Consistency Trajectory Loss is derived as follows:

$$\begin{aligned}
 L_{CTS} &= \mathbb{E}[\|w_1(t)(\epsilon_\theta(x_{s \rightarrow t}, t, y) - \epsilon_\theta(x_s, s, \emptyset))\|_2^2 + \|w_2(s, t)(\epsilon_\theta(x_s, s, \emptyset) - \epsilon)\|_2^2] \\
 w_1(t) &= c_{out}(t) \left(\frac{\sigma_t}{\alpha_t} \right) \\
 w_2(s, t) &= [c_{out}(t) - c_{out}(s)] \left(\frac{\sigma_s}{\alpha_s} \right)
 \end{aligned} \tag{5}$$

where $t > s$ are two adjacent diffusion time steps, $x_s = \alpha_s x_\pi + \sigma_s \epsilon$, and $x_{s \rightarrow t}$ is a less noisy sample derived from deterministic sampling by running one discretization step of a ODE solver from x_s . ϵ is the random noise that will only be sampled once and kept fixed. y is the text condition.

Justification. In the following, we offer two theoretical justifications to demonstrate that, our CTS loss is equivalent to the Consistency Loss Song et al. [2023] and upon achieving convergence, our CTS loss is capable of generating a high-fidelity 3D model.

Theorem 1 Let $f_\theta(\cdot)(x, t)$ denote the pre-trained consistency function. We assume $f_\theta(\cdot)$ satisfies the formulation defined in Latent Consistency Model Luo et al. [2023], and $t \geq 30$. Assume further that for all $t \geq 30$, the ODE solver G called at t_{n+1} has local error uniformly bounded by $O((\Delta t)^{p+1})$ with $p \geq 1$. The Consistency Loss Luo et al. [2023] can be mathematically expressed as the sum of the Consistency Trajectory Sampling Loss and one infinitesimal components, along with a term whose

magnitude is bounded by 10^{-7} :

$$L_{CD} = L_{CTS} + \underbrace{\left(-\frac{O((\Delta t)^2)}{\alpha_{t_{n+1}}}\right) + c_{skip}(t_{n+1})O((\Delta t)^{p+1})}_{\text{infinitesimal components}} + \underbrace{m}_{|m| \leq 10^{-7}} \quad (6)$$

$$= L_{CTS} + O((\Delta t)^2) + m$$

where $c_{skip}(\cdot), c_{out}(\cdot)$ is coefficient in consistency function.

Theorem 2 Assume that the pre-trained noise predictor $\epsilon_\theta(\cdot; \cdot)$ in Consistency Model Luo et al. [2023], Song et al. [2023] satisfies the Lipschitz condition. Define $\Delta := \sup\{|t_n - t_{n+1}|\}$. For any given camera pose π , if convergence is achieved according to L_{CTS} , then there exists a corresponding real image $x_0 \sim p_{data}(x)$ such that:

$$\|x_\pi - x_0\|_2 = O(\Delta) \quad (7)$$

where $x_\pi = g(\theta, \pi)$ denotes the rendered image for pose π .

In addition, we can proof that the existing methods Chen et al. [2024b], Zhong et al. [2024] which incorporate Consistency Model Song et al. [2023] can be amalgamated into our framework. We provide the full proof in Appendix.

Theorem 3 guarantees that the CTS loss function comprehensively inherits the capability of the Consistency model, while Theorem 4 demonstrates that images synthesized by our framework exhibit both photorealism and semantic alignment with real-world environments.

Once 3DGS developed distinct semantic signal which align with the text prompts, adding noise drives the model to alter details for text alignment. However, as most text lack high-frequency specifics, the focus should be on enhancing detail generation rather than forces alignment. Therefore, we remove the noise and the second term of L_{CTS} , and set $x_s = x_\pi$ when $t \leq 500$ as shown in Figure 3. To constrain the furniture to maintain scale, position align with the provided layout priors, we introduce the bounding box loss:

$$L_{Layout} = d^x(G_x, x_i, h_i) + d^y(G_y, y_i, w_i) + d^z(G_z, z_i, l_i) \quad (8)$$

$$d^x(G_x, x_i, h_i) = \|\min(G_x) - (x_i - \frac{h_i}{2})\|_2^2 + \|\max(G_x) - (x_i + \frac{h_i}{2})\|_2^2$$

where G_x is a set of furniture Gaussian center μ on the x-axis, x_i is the position of the layout center on the x-axis, and h_i is the height of the layout prior to the i-the furniture. Additionally, we incorporate L_{scale} and L_{normal} for texture detail enhancement. Further details be found in the Supplementary Material.

4.3 Environment Optimization

After obtaining furniture, we place the furniture into 3D layout and start optimizing environment. Previous methods directly optimize latent map with the SDS loss Chen et al. [2024a] or iteratively inpaint the missing texture in each viewpoint. While optimization-based approaches often suffer from multi-view geometric inconsistencies due to gradient conflicts across viewpoints, inpainting-based methods exhibit limitations in synthesizing high-frequency texture detail and geometrically plausible ornaments (e.g., wall moldings, cornices). In this section, we begin by introducing a multi-resolution texture field module and a normal-aware decoder to synthesize visually coherent and spatially consistent texture. Subsequently, we propose a zigzag adaptive camera trajectory to address environment optimization across multiple spatial scales and apply CTS loss for realistic texture generation.

4.3.1 Texture Field & Decoder

To tackle those inherent disadvantages, we adopt a multi-resolution texture field that queries the texture features with given UV coordinates Chen et al. [2024a]. We encode texture features for all UV coordinate q at each scale, and concatenate those features as the output UV embeddings $\varepsilon(q)$ to faithfully represent all texture details. Then the UV embeddings are decoded to the final RGB value by the cross-attention texture decoder. Motivated by the empirical observation that consistent normal correlate with texture style divergence, inconsistent normal correlate with texture style consistency,



Figure 5: Qualitative comparisons of SceneLCM and baselines. Set-the-SceneCohen-Bar et al. [2023] and Text2RoomHöllein et al. [2023] generate incomplete results; The floorplan of DreamSceneLi et al. [2024a] is automatically generated and the environment exhibits multi-view inconsistency, with floor and bed fused together in column five; SceneCraftYang et al. [2024a] generates incorrect style outputs and blurry images. Our method is capable of producing highly detailed scenes, including realistic floor textures, while simultaneously generating wall decorations such as curtains and windows.



Figure 6: Generation results of SceneLCM in multi-room. The left column represents the layout, where we distill the multi-resolution texture field on a 4096×4096 texture map serving as the texture map of layout. We demonstrate SceneLCM’s ability to generate more complex indoor scenes.

we propose an effective rendering module with normal awareness to predict RGB values. Specifically, for each rasterized UV coordinate, we apply a UV instance mask to mask out instance with the same normal. Then, we obtain the UV embeddings for the rasterized locations in the view. Meanwhile, we extract the texture features for the pre-sampled UVs scattered across this instances with same normal as the reference UV embeddings as shown in Figure. 4. We deploy a multi-head cross-attention module to produce the instance-aware UV embeddings. Followed SceneTexChen et al. [2024a], we treat the rendering UV embeddings as Query, and the reference UV embeddings as Key and Value. Finally, a shared MLP projects the UV embeddings to RGB values. We denote the whole rendering process as $C = M(\varepsilon(q); \phi)$, where C represents an RGB image arbitrary resolution, $M(\cdot; \phi)$ is a differentiable function resembles the entire texture field and decoder with trainable parameters ϕ .

4.3.2 Texture Optimization

We adopt a LCMLuo et al. [2023] as a critic to optimize the texturing module following the strategy of SceneTexChen et al. [2024a]. We render RGB image via querying the texture field $C = M(\varepsilon(q); \phi)$. In each iteration, optimize C via the CTS objective with a pre-trained frozen depth-conditioned

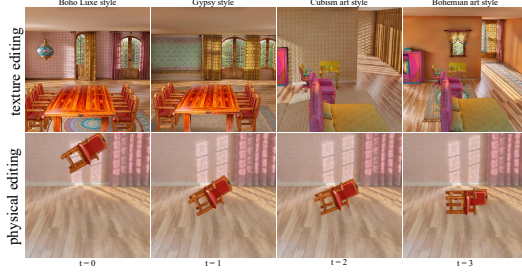


Figure 7: Editing Results.

diffusion ϵ_θ :

$$\nabla_\phi L_{CTS} = \mathbb{E}_{t,\epsilon} [(|w_1(t)(\epsilon_\theta(x_{s \rightarrow t}, t, y, x_\pi^d) - \epsilon_\theta(x_s, s, \emptyset))| + |w_2(s, t)(\epsilon_\theta(x_s, s, \emptyset) - \epsilon)|) \frac{\partial M(\epsilon(q); \phi)}{\partial \phi}] \quad (9)$$

where $x_s = \alpha_s x_\pi + \sigma_s \epsilon$, $x_\pi = M(\epsilon(q); \phi)$ and x_π^d is the depth map of x_π . We also remove the noise after $t \leq 500$.

Unlike previous methods Chen et al. [2024a], Wang et al. [2024a], Huang et al. [2024b], we focus on multi-room settings. Direct application of CTS loss often introduces patchy artifacts and incomplete texture maps, stemming from ultra-dense UV parameterization causing adjacent UV coordinates to exhibit tight numerical proximity and unstable camera trajectories. These numerical proximities induce pathological initializations, leading to local optima and unstable camera trajectories that fail to capture global scenes at large scales.

To address those issues, we treat UV coordinates as spherical coordinates and convert them to cartesian coordinates, while applying layernorm after each UV embedding to amplify inter-data distinctions. We propose a zigzag adaptive camera trajectory where the camera and target closely follow walls during motions. Specifically, the camera’s xy coordinates move in the opposite direction to those of the target, while its height is inversely proportional to the target’s height.

5 Experiments

Implementation Details. We utilized GPT-4 Achiam et al. [2023] as our LLM for 3D layout generation, latent consistency model Luo et al. [2023] as our diffusion model, Point-E for initial representation of objects. We tested SceneLCM and all the baselines on the A800 GPU for fair comparison.

Baselines. For the comparison of the scene generation, we use the current open-sourced SOTA methods Text2Room Höllein et al. [2023], set-the-scene Cohen-Bar et al. [2023], DreamScene Li et al. [2024a] and SceneCraft Yang et al. [2024a]. For text-to-3D generation, we select open-source SOTA methods luciddreamer Liang et al. [2024], vividreamer Chen et al. [2024b], CCD Li et al. [2024b] and DreamScene Li et al. [2024a].

Evaluation Metrics We tested the generation time of each method Höllein et al. [2023], Cohen-Bar et al. [2023], Li et al. [2024a], Yang et al. [2024a], compared the editing and generative capabilities against their published papers, and did a 20-participant user study to score (out of ten) the quality of the videos generated by each method for 3 scenes of 15 seconds.

5.1 Qualitative Results

Indoor Scene. Figure 5 shows the comparison of SceneLCM with the SOTA. We rotated the camera to capture a 360-degree scene, demonstrating our consistency. Text2Room Zhang et al. [2024b] uses the text-conditioned inpainting model to generate frame by frame and only produces satisfactory results under camera poses encountered. Set-the-Scene Cohen-Bar et al. [2023] is a Nerf-composition methods that lacks the capability to generate objects with varying scales, resulting in blurred results. SceneCraft Yang et al. [2024a] finetunes a 2D diffusion model conditioned on bounding-box images, and apply a SDS loss for scene optimization. Our generated layouts are incompatible with SceneCraft’s native format, so we create layouts for SceneCraft manually to align with ours as closely as possible. Due to the insufficient capacity of the SceneCraft-finetuned diffusion model, it struggles to reason the layouts which contain many closely placed objects.

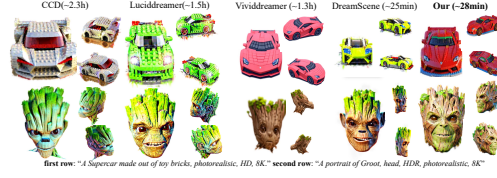


Figure 8: Comparison with baselines in text-to-3D generation.

DreamSceneLi et al. [2024a] employs Formation Pattern Sampling for objects generation, and a progressive three-stage camera sampling strategy to effectively ensure object and environment integration. DreamScene exclusively processes relative spatial relationships between objects to autonomously generate floorplans. Due to DreamSceneLi et al. [2024a] lacks of geometric constraints in environment, the resulting environments typically exhibit multi-view inconsistency. For example, in the second row of the sixth column of Figure 5, the floor and bed are seamlessly integrated into a unified structure. Additionally, the unrestricted proliferation of Gaussians induces unrealistic visual artifacts. In contrast, our model addresses all these issues: It can generate complex and realistic scenes while ensuring multi-view consistency.

Objects. Figure 8 shows that our CTS can generate realistic 3D representation following the text prompt in a short time. DreamSceneLi et al. [2024a] is fastest yet at the cost of low generation quality.

More Results. In Figure 6, we showcase the results of multi-room generation with full layout on the free-camera trajectory. Users only need to input text, and our end-to-end model autonomously generates entire houses with distinct styles per room, requiring zero human intervention throughout the entire generation process.

Editing. In Figure 7, we show 4 variants of generation with two room layouts and different appearance, simply achieved by using different texture map of environment in first row. In second row, we show that our model can support physically plausible editing. A chair in mid-air will fall downward under gravitational force.

5.2 Quantitative Results

Since baselines Yang et al. [2024a], Höllein et al. [2023], Cohen-Bar et al. [2023] are not able to generate objects in the environment independently, for a fair comparison we calculate the generation time of our environment generation stage per room. The left side of Table 1 shows that we have robust editing capabilities and the right side shows the user study, where SceneLCM is far ahead of baselines in terms of quality.

5.3 Ablation Study

The appendix section offers a comprehensive introduction to all of our evaluated models and additional experimental details. Please refer to Appendix for more details.

6 Limitation and Conclusion

SceneLCM currently exhibits limitations in generating high-fidelity layout arrangements (e.g., books on shelves, cups on tables) as ArchitectWang et al. [2024b]. Secondly, our CTS loss still suffers from the Janus issue, causing dualistic artifacts.

In summary, we introduce an novel end-to-end indoor scene generative framework. By employing layout refine strategy, Consistency Trajectory Sampling(CTS), texture field and normal-aware decoder for environment optimization, we address the current issues of inefficiency, inconsistency, single-room generation, and limited physical editability in current text-to-3D scene generation methods. Extensive experiments have demonstrated that SceneLCM is a milestone achievement in 3D scene generation, holding potential for wide ranging applications across numerous fields.

References

- Josh Achiam, Steven Adler, Sandhini Agarwal, Lama Ahmad, Ilge Akkaya, Florencia Leoni Aleman, Diogo Almeida, Janko Altschmidt, Sam Altman, Shyamal Anadkat, et al. Gpt-4 technical report. *arXiv preprint arXiv:2303.08774*, 2023.
- Mohammadreza Armandpour, Ali Sadeghian, Huangjie Zheng, Amir Sadeghian, and Mingyuan Zhou. Re-imagine the negative prompt algorithm: Transform 2d diffusion into 3d, alleviate janus problem and beyond. *arXiv preprint arXiv:2304.04968*, 2023.
- Tom Brown, Benjamin Mann, Nick Ryder, Melanie Subbiah, Jared D Kaplan, Prafulla Dhariwal, Arvind Neelakantan, Pranav Shyam, Girish Sastry, Amanda Askell, et al. Language models are few-shot learners. *Advances in neural information processing systems*, 33:1877–1901, 2020.

- Dave Zhenyu Chen, Haoxuan Li, Hsin-Ying Lee, Sergey Tulyakov, and Matthias Nießner. Scenetex: High-quality texture synthesis for indoor scenes via diffusion priors. In *Proceedings of the IEEE/CVF Conference on Computer Vision and Pattern Recognition*, pages 21081–21091, 2024a.
- Hansheng Chen, Jiatao Gu, Anpei Chen, Wei Tian, Zhuowen Tu, Lingjie Liu, and Hao Su. Single-stage diffusion nerf: A unified approach to 3d generation and reconstruction. In *Proceedings of the IEEE/CVF international conference on computer vision*, pages 2416–2425, 2023a.
- Rui Chen, Yongwei Chen, Ningxin Jiao, and Kui Jia. Fantasia3d: Disentangling geometry and appearance for high-quality text-to-3d content creation. In *Proceedings of the IEEE/CVF international conference on computer vision*, pages 22246–22256, 2023b.
- Zixuan Chen, Ruijie Su, Jiahao Zhu, Lingxiao Yang, Jian-Huang Lai, and Xiaohua Xie. Vividdreamer: Towards high-fidelity and efficient text-to-3d generation. *arXiv preprint arXiv:2406.14964*, 2024b.
- Dana Cohen-Bar, Elad Richardson, Gal Metzer, Raja Giryes, and Daniel Cohen-Or. Set-the-scene: Global-local training for generating controllable nerf scenes. In *Proceedings of the IEEE/CVF International Conference on Computer Vision*, pages 2920–2929, 2023.
- Blender Online Community. *Blender - a 3D modelling and rendering package*. Blender Foundation, Stichting Blender Foundation, Amsterdam, 2018. URL <http://www.blender.org>.
- Wei Deng, Mengshi Qi, and Huadong Ma. Global-local tree search in vlms for 3d indoor scene generation. *arXiv preprint arXiv:2503.18476*, 2025.
- Epic Games. Unreal engine. URL <https://www.unrealengine.com>.
- Rao Fu, Zehao Wen, Zichen Liu, and Srinath Sridhar. Anyhome: Open-vocabulary generation of structured and textured 3d homes. In *European Conference on Computer Vision*, pages 52–70. Springer, 2024.
- Ian J Goodfellow, Jean Pouget-Abadie, Mehdi Mirza, Bing Xu, David Warde-Farley, Sherjil Ozair, Aaron Courville, and Yoshua Bengio. Generative adversarial nets. *Advances in neural information processing systems*, 27, 2014.
- Antoine Guédon and Vincent Lepetit. Sugar: Surface-aligned gaussian splatting for efficient 3d mesh reconstruction and high-quality mesh rendering. In *Proceedings of the IEEE/CVF Conference on Computer Vision and Pattern Recognition*, pages 5354–5363, 2024.
- Daya Guo, Dejian Yang, Haowei Zhang, Junxiao Song, Ruoyu Zhang, Runxin Xu, Qihao Zhu, Shirong Ma, Peiyi Wang, Xiao Bi, et al. Deepseek-r1: Incentivizing reasoning capability in llms via reinforcement learning. *arXiv preprint arXiv:2501.12948*, 2025.
- Jonathan Ho and Tim Salimans. Classifier-free diffusion guidance. In *NeurIPS 2021 Workshop on Deep Generative Models and Downstream Applications*, 2021.
- Jonathan Ho, Ajay Jain, and Pieter Abbeel. Denoising diffusion probabilistic models. *Advances in neural information processing systems*, 33:6840–6851, 2020.
- Lukas Höllein, Ang Cao, Andrew Owens, Justin Johnson, and Matthias Nießner. Text2room: Extracting textured 3d meshes from 2d text-to-image models. In *Proceedings of the IEEE/CVF International Conference on Computer Vision*, pages 7909–7920, 2023.
- Binbin Huang, Zehao Yu, Anpei Chen, Andreas Geiger, and Shenghua Gao. 2d gaussian splatting for geometrically accurate radiance fields. In *ACM SIGGRAPH 2024 conference papers*, pages 1–11, 2024a.
- Yukun Huang, Jianan Wang, Yukai Shi, Boshi Tang, Xianbiao Qi, and Lei Zhang. Dreamtime: An improved optimization strategy for diffusion-guided 3d generation. In *The Twelfth International Conference on Learning Representations*.
- Zhipeng Huang, Wangbo Yu, Xinhua Cheng, ChengShu Zhao, Yunyang Ge, Mingyi Guo, Li Yuan, and Yonghong Tian. Roompainter: View-integrated diffusion for consistent indoor scene texturing. *arXiv preprint arXiv:2412.16778*, 2024b.

- Ka-Hei Hui, Ruihui Li, Jingyu Hu, and Chi-Wing Fu. Neural wavelet-domain diffusion for 3d shape generation. In *SIGGRAPH Asia 2022 Conference Papers*, pages 1–9, 2022.
- Bernhard Kerbl, Georgios Kopanas, Thomas Leimkühler, and George Drettakis. 3d gaussian splatting for real-time radiance field rendering. *ACM Trans. Graph.*, 42(4):139–1, 2023.
- Haoran Li, Haolin Shi, Wenli Zhang, Wenjun Wu, Yong Liao, Lin Wang, Lik-hang Lee, and Peng Yuan Zhou. Dreamscene: 3d gaussian-based text-to-3d scene generation via formation pattern sampling. In *European Conference on Computer Vision*, pages 214–230. Springer, 2024a.
- Zongrui Li, Minghui Hu, Qian Zheng, and Xudong Jiang. Connecting consistency distillation to score distillation for text-to-3d generation. In *European Conference on Computer Vision*, pages 274–291. Springer, 2024b.
- Yixun Liang, Xin Yang, Jiantao Lin, Haodong Li, Xiaogang Xu, and Yingcong Chen. Luciddreamer: Towards high-fidelity text-to-3d generation via interval score matching. In *Proceedings of the IEEE/CVF conference on computer vision and pattern recognition*, pages 6517–6526, 2024.
- Chen-Hsuan Lin, Jun Gao, Luming Tang, Towaki Takikawa, Xiaohui Zeng, Xun Huang, Karsten Kreis, Sanja Fidler, Ming-Yu Liu, and Tsung-Yi Lin. Magic3d: High-resolution text-to-3d content creation. In *Proceedings of the IEEE/CVF conference on computer vision and pattern recognition*, pages 300–309, 2023.
- Chenguo Lin and Yadong Mu. Instructscene: Instruction-driven 3d indoor scene synthesis with semantic graph prior. In *International Conference on Learning Representations (ICLR)*, 2024.
- Aixin Liu, Bei Feng, Bing Xue, Bingxuan Wang, Bochao Wu, Chengda Lu, Chenggang Zhao, Chengqi Deng, Chenyu Zhang, Chong Ruan, et al. Deepseek-v3 technical report. *arXiv preprint arXiv:2412.19437*, 2024.
- Tao Lu, Mulin Yu, Linning Xu, Yuanbo Xiangli, Limin Wang, Dahua Lin, and Bo Dai. Scaffold-gs: Structured 3d gaussians for view-adaptive rendering. In *Proceedings of the IEEE/CVF Conference on Computer Vision and Pattern Recognition*, pages 20654–20664, 2024.
- Shitong Luo and Wei Hu. Diffusion probabilistic models for 3d point cloud generation. In *Proceedings of the IEEE/CVF conference on computer vision and pattern recognition*, pages 2837–2845, 2021.
- Simian Luo, Yiqin Tan, Longbo Huang, Jian Li, and Hang Zhao. Latent consistency models: Synthesizing high-resolution images with few-step inference. *arXiv preprint arXiv:2310.04378*, 2023.
- Ben Mildenhall, Pratul P Srinivasan, Matthew Tancik, Jonathan T Barron, Ravi Ramamoorthi, and Ren Ng. Nerf: Representing scenes as neural radiance fields for view synthesis. *Communications of the ACM*, 65(1):99–106, 2021.
- Alex Nichol, Heewoo Jun, Prafulla Dhariwal, Pamela Mishkin, and Mark Chen. Point-e: A system for generating 3d point clouds from complex prompts. *arXiv preprint arXiv:2212.08751*, 2022.
- Jeong Joon Park, Peter Florence, Julian Straub, Richard Newcombe, and Steven Lovegrove. DeepSDF: Learning continuous signed distance functions for shape representation. In *Proceedings of the IEEE/CVF conference on computer vision and pattern recognition*, pages 165–174, 2019.
- Ben Poole, Ajay Jain, Jonathan T Barron, and Ben Mildenhall. Dreamfusion: Text-to-3d using 2d diffusion. *arXiv preprint arXiv:2209.14988*, 2022.
- Nikhila Ravi, Jeremy Reizenstein, David Novotny, Taylor Gordon, Wan-Yen Lo, Justin Johnson, and Georgios Gkioxari. Accelerating 3d deep learning with pytorch3d. *arXiv:2007.08501*, 2020.
- Xuanchi Ren, Jiahui Huang, Xiaohui Zeng, Ken Museth, Sanja Fidler, and Francis Williams. Xcube: Large-scale 3d generative modeling using sparse voxel hierarchies. In *Proceedings of the IEEE/CVF conference on computer vision and pattern recognition*, pages 4209–4219, 2024.

- Jonas Schult, Sam Tsai, Lukas Höllein, Bichen Wu, Jialiang Wang, Chih-Yao Ma, Kunpeng Li, Xiaofang Wang, Felix Wimbauer, Zijian He, et al. Controlroom3d: Room generation using semantic proxy rooms. In *Proceedings of the IEEE/CVF Conference on Computer Vision and Pattern Recognition*, pages 6201–6210, 2024.
- Yichun Shi, Peng Wang, Jianglong Ye, Long Mai, Kejie Li, and Xiao Yang. Mvdream: Multi-view diffusion for 3d generation. In *The Twelfth International Conference on Learning Representations*.
- Yang Song, Prafulla Dhariwal, Mark Chen, and Ilya Sutskever. Consistency models. In *Proceedings of the 40th International Conference on Machine Learning*, pages 32211–32252, 2023.
- Unity Technologies. Unity, 2023. URL <https://unity.com/>. Game development platform.
- Arash Vahdat, Francis Williams, Zan Gojcic, Or Litany, Sanja Fidler, Karsten Kreis, et al. Lion: Latent point diffusion models for 3d shape generation. *Advances in Neural Information Processing Systems*, 35:10021–10039, 2022.
- Haochen Wang, Xiaodan Du, Jiahao Li, Raymond A Yeh, and Greg Shakhnarovich. Score jacobian chaining: Lifting pretrained 2d diffusion models for 3d generation. In *Proceedings of the IEEE/CVF conference on computer vision and pattern recognition*, pages 12619–12629, 2023a.
- Qi Wang, Ruijie Lu, Xudong Xu, Jingbo Wang, Michael Yu Wang, Bo Dai, Gang Zeng, and Dan Xu. Roomtex: Texturing compositional indoor scenes via iterative inpainting. In *European Conference on Computer Vision*, pages 465–482. Springer, 2024a.
- Yian Wang, Xiaowen Qiu, Jiageng Liu, Zhehuan Chen, Jiting Cai, Yufei Wang, Tsun-Hsuan Johnson Wang, Zhou Xian, and Chuang Gan. Architect: Generating vivid and interactive 3d scenes with hierarchical 2d inpainting. *Advances in Neural Information Processing Systems*, 37:67575–67603, 2024b.
- Zhengyi Wang, Cheng Lu, Yikai Wang, Fan Bao, Chongxuan Li, Hang Su, and Jun Zhu. Pro-lificdreamer: High-fidelity and diverse text-to-3d generation with variational score distillation. *Advances in Neural Information Processing Systems*, 36:8406–8441, 2023b.
- Shuang Wu, Youtian Lin, Feihu Zhang, Yifei Zeng, Jingxi Xu, Philip Torr, Xun Cao, and Yao Yao. Direct3d: Scalable image-to-3d generation via 3d latent diffusion transformer. *Advances in Neural Information Processing Systems*, 37:121859–121881, 2024a.
- Zike Wu, Pan Zhou, Xuanyu Yi, Xiaoding Yuan, and Hanwang Zhang. Consistent3d: Towards consistent high-fidelity text-to-3d generation with deterministic sampling prior. In *Proceedings of the IEEE/CVF Conference on Computer Vision and Pattern Recognition*, pages 9892–9902, 2024b.
- Jianfeng Xiang, Zelong Lv, Sicheng Xu, Yu Deng, Ruicheng Wang, Bowen Zhang, Dong Chen, Xin Tong, and Jiaolong Yang. Structured 3d latents for scalable and versatile 3d generation. *arXiv preprint arXiv:2412.01506*, 2024.
- Runjie Yan, Yinbo Chen, and Xiaolong Wang. Consistent flow distillation for text-to-3d generation. *arXiv preprint arXiv:2501.05445*, 2025.
- Xiuyu Yang, Yunze Man, Junkun Chen, and Yu-Xiong Wang. Scenecraft: Layout-guided 3d scene generation. *Advances in Neural Information Processing Systems*, 37:82060–82084, 2024a.
- Yue Yang, Fan-Yun Sun, Luca Weihs, Eli VanderBilt, Alvaro Herrasti, Winson Han, Jiajun Wu, Nick Haber, Ranjay Krishna, Lingjie Liu, et al. Holodeck: Language guided generation of 3d embodied ai environments. In *CVPR*, 2024b.
- Zehao Yu, Anpei Chen, Binbin Huang, Torsten Sattler, and Andreas Geiger. Mip-splatting: Alias-free 3d gaussian splatting. In *Proceedings of the IEEE/CVF conference on computer vision and pattern recognition*, pages 19447–19456, 2024.
- Guangyao Zhai, Evin Pinar Örneke, Dave Zhenyu Chen, Ruotong Liao, Yan Di, Nassir Navab, Federico Tombari, and Benjamin Busam. Echoscene: Indoor scene generation via information echo over scene graph diffusion. In *European Conference on Computer Vision*, pages 167–184. Springer, 2024.

- Baowen Zhang, Chuan Fang, Rakesh Shrestha, Yixun Liang, Xiaoxiao Long, and Ping Tan. Rade-gs: Rasterizing depth in gaussian splatting. *arXiv preprint arXiv:2406.01467*, 2024a.
- Biao Zhang, Jiapeng Tang, Matthias Niessner, and Peter Wonka. 3dshape2vecset: A 3d shape representation for neural fields and generative diffusion models. *ACM Transactions On Graphics (TOG)*, 42(4):1–16, 2023.
- Jingbo Zhang, Xiaoyu Li, Ziyu Wan, Can Wang, and Jing Liao. Text2nerf: Text-driven 3d scene generation with neural radiance fields. *IEEE Transactions on Visualization and Computer Graphics*, 30(12):7749–7762, 2024b.
- Longwen Zhang, Ziyu Wang, Qixuan Zhang, Qiwei Qiu, Anqi Pang, Haoran Jiang, Wei Yang, Lan Xu, and Jingyi Yu. Clay: A controllable large-scale generative model for creating high-quality 3d assets. *ACM Transactions on Graphics (TOG)*, 43(4):1–20, 2024c.
- Zibo Zhao, Wen Liu, Xin Chen, Xianfang Zeng, Rui Wang, Pei Cheng, Bin Fu, Tao Chen, Gang Yu, and Shenghua Gao. Michelangelo: Conditional 3d shape generation based on shape-image-text aligned latent representation. *Advances in neural information processing systems*, 36:73969–73982, 2023.
- Yiming Zhong, Xiaolin Zhang, Yao Zhao, and Yunchao Wei. Dreamlcm: Towards high quality text-to-3d generation via latent consistency model. In *Proceedings of the 32nd ACM International Conference on Multimedia*, pages 1731–1740, 2024.
- Xiaoyu Zhou, Xingjian Ran, Yajiao Xiong, Jinlin He, Zhiwei Lin, Yongtao Wang, Deqing Sun, and Ming-Hsuan Yang. Gala3d: Towards text-to-3d complex scene generation via layout-guided generative gaussian splatting. In *International Conference on Machine Learning*, pages 62108–62118. PMLR, 2024.
- Junzhe Zhu, Peiye Zhuang, and Sanmi Koyejo. Hifa: High-fidelity text-to-3d generation with advanced diffusion guidance. In *The Twelfth International Conference on Learning Representations*.

7 Supplement Detail

- Theoretical Proof 7.1.1
- Pipeline Detail 7.2
- Discussion for Related Work 7.3
- Explanation of Experiments 7.4
- Additional Experiments 7.5
- Ablation Study 7.6

7.1 Theoretical Proof

We first prove two theorems and one corollary, then conduct ablation studies to demonstrate that the m exerts no influence on the experimental results.

7.1.1 Theoretical Proof

Theorem 3 Let $f_\theta(\cdot)(x, t)$ denote the pre-trained consistency function. We assume $f_\theta(\cdot)$ satisfies the formulation defined in Latent Consistency Model Luo et al. [2023], and $t \geq 30$. Assume further that for all $t \geq 30$, the ODE solver G called at t_{n+1} has local error uniformly bounded by $O((t_{n+1} - t_n)^{p+1})$ with $p \geq 1$. The Consistency Loss Luo et al. [2023] can be mathematically expressed as the sum of the Consistency Trajectory Sampling Loss and two infinitesimal components, along with a term whose magnitude is bounded by 10^{-7} :

$$\begin{aligned}
 L_{CD} &= L_{CTS} + \underbrace{\left(-\frac{O(h^2)}{\alpha_{t_{n+1}}}\right) + c_{skip}(t_{n+1})O((\Delta t)^{p+1})}_{\text{infinitesimal components}} + \underbrace{m}_{|m| \leq 10^{-7}} \\
 &= o((\Delta t)^2) + m \\
 h &= \log\left(\frac{\alpha_{t_n}}{\sigma_{t_n}}\right) - \log\left(\frac{\alpha_{t_{n+1}}}{\sigma_{t_{n+1}}}\right)
 \end{aligned} \tag{10}$$

Proof The proof is based on the formulation defined in Latent Consistency Model Luo et al. [2023]. We have $f_\theta(x, t) = c_{skip}(t)x + c_{out}(t)F_\theta(x_t, t)$, where $F_\theta(x_t, t) = \frac{x_t - \sigma_t \epsilon_\theta(x_t, t)}{\alpha_t}$, $c_{skip}(t) = \frac{\sigma^2}{(\frac{t}{0.1})^2 + \sigma^2}$, $c_{out}(t) = \frac{\frac{t}{0.1}}{\sqrt{(\frac{t}{0.1})^2 + \sigma^2}}$, and $\sigma = \frac{1}{2}$. x_t is obtained by ODE solver applied to x_s . To simplicity, we omit the condition c of the consistency function and exponential moving average (EMA) of the parameter θ . We use the DPM-solver as ODE solver $G(x_s, s, t)$, $x_{s \rightarrow t} = G(x_s, s, t)$, where $x_{s \rightarrow t}$ is obtained by ODE solver from s to t .

For simplicity, the absolute value notation is omitted in following derivation.

$$\begin{aligned}
 L_{CD} &= \|f_\theta(x_{t_n}, t_n) - f_\theta(x_{t_n \rightarrow t_{n+1}}, t_{n+1})\|_2^2 \\
 &= c_{skip}(t_n)x_{t_n} + c_{out}(t_n)F_\theta(x_{t_n}, t_n) - c_{skip}(t_{n+1})x_{t_n \rightarrow t_{n+1}} - c_{out}(t_{n+1})F_\theta(x_{t_n \rightarrow t_{n+1}}, t_{n+1}) \\
 &= \underbrace{[c_{skip}(t_n)x_{t_n} - c_{skip}(t_{n+1})x_{t_n \rightarrow t_{n+1}}]}_{\text{term 1}} + \underbrace{c_{out}(t_n)[F_\theta(x_{t_n}, t_n) - F_\theta(x_{t_n \rightarrow t_{n+1}}, t_{n+1})]}_{\text{term 2}} \\
 &\quad + \underbrace{[c_{out}(t_n) - c_{out}(t_{n+1})]F_\theta(x_{t_n \rightarrow t_{n+1}}, t_{n+1})}_{\text{term 3}}
 \end{aligned} \tag{11}$$

where $x_{t_n \rightarrow t_{n+1}}$ is calculated given ODE solver G as $x_{t_n \rightarrow t_{n+1}} = G(x_{t_n}; t_n, t_{n+1})$.

term 1:

$$\begin{aligned}
[c_{skip}(t_n)x_{t_n} - c_{skip}(t_{n+1})x_{t_n \rightarrow t_{n+1}}] &= c_{skip}(t_n)x_{t_n} - c_{skip}(t_{n+1})G(x_{t_n}; t_n, t_{n+1}) \\
&= c_{skip}(t_n)x_{t_n} - c_{skip}(t_{n+1})(G(x_{t_n}; t_n, t_{n+1}) - x_{t_{n+1}} + x_{t_{n+1}}) \\
&= [c_{skip}(t_n)x_{t_n} - c_{skip}(t_{n+1})x_{t_{n+1}}] + c_{skip}(t_{n+1})(x_{t_{n+1}} - G(x_{t_n}; t_n, t_{n+1})) \\
&\leq c_{skip}(t_n)(\alpha_{t_n}x_{\pi} + \sigma_{t_n}\epsilon) - c_{skip}(t_{n+1})(\alpha_{t_{n+1}}x_{\pi} + \sigma_{t_{n+1}}\epsilon) \\
&\quad + c_{skip}(t_{n+1})\underbrace{O((t_n - t_{n+1})^{p+1})}_{\text{local error of Euler solver}} \\
&= (c_{skip}(t_n)\alpha_{t_n} - c_{skip}(t_{n+1})\alpha_{t_{n+1}})x_{\pi} \\
&\quad + [c_{skip}(t_n)\sigma_{t_n} - c_{skip}(t_{n+1})\sigma_{t_{n+1}}]\epsilon \\
&\quad + c_{skip}(t_{n+1})O((\Delta t)^{p+1})
\end{aligned} \tag{12}$$

where $0 < \alpha_{t_n}, \sigma_{t_n} < 1$. When $t \geq 30$, $c_{skip}(t)$ is monotonically decreasing, and $0 < c_{skip}(t)\alpha_t \leq 10^{-7}$. Because all experiments were conducted under FP16 configuration, $c_{skip}(t)\alpha_t, c_{skip}(t)\sigma_t \approx 0$. Beside, t exceeds 100 in the vast majority of cases. term 1 can be simplified as:

$$[c_{skip}(t_n)x_{t_n} - c_{skip}(t_{n+1})x_{t_n \rightarrow t_{n+1}}] = m + c_{skip}(t_{n+1})O((\Delta t)^{p+1}) \tag{13}$$

where m is a value so small that it is effectively negligible in devices.

term 2: We use the DPM-solver as ODE solver $G(x_s, s, t)$:

$$\begin{aligned}
[F_{\theta}(x_{t_n}, t_n) - F_{\theta}(x_{t_n \rightarrow t_{n+1}}, t_{n+1})] &= \frac{x_{t_n} - \sigma_{t_n}\epsilon_{\theta}(x_{t_n}, t_n)}{\alpha_{t_n}} - \frac{x_{t_n \rightarrow t_{n+1}} - \sigma_{t_{n+1}}\epsilon_{\theta}(x_{t_n \rightarrow t_{n+1}}, t_{n+1})}{\alpha_{t_{n+1}}} \\
&= \frac{x_{t_n} - \sigma_{t_n}\epsilon_{\theta}(x_{t_n}, t_n)}{\alpha_{t_n}} \\
&\quad - \frac{\frac{\alpha_{t_{n+1}}}{\alpha_{t_n}}x_{t_n} - \sigma_{t_{n+1}}(e^{-h} - 1)\epsilon_{\theta}(x_{t_n}, t_n) + O(h^2) - \sigma_{t_{n+1}}\epsilon_{\theta}(x_{t_n \rightarrow t_{n+1}}, t_{n+1})}{\alpha_{t_{n+1}}} \\
&= \frac{x_{t_n} - \sigma_{t_n}\epsilon_{\theta}(x_{t_n}, t_n)}{\alpha_{t_n}} \\
&\quad - \frac{\frac{\alpha_{t_{n+1}}}{\alpha_{t_n}}x_{t_n} - \alpha_{t_{n+1}}(\frac{\sigma_{t_n}}{\alpha_{t_n}} - \frac{\sigma_{t_{n+1}}}{\alpha_{t_{n+1}}})\epsilon_{\theta}(x_{t_n}, t_n) + O(h^2) - \sigma_{t_{n+1}}\epsilon_{\theta}(x_{t_n \rightarrow t_{n+1}}, t_{n+1})}{\alpha_{t_{n+1}}} \\
&= \frac{x_{t_n} - \sigma_{t_n}\epsilon_{\theta}(x_{t_n}, t_n)}{\alpha_{t_n}} \\
&\quad - (\frac{x_{t_n}}{\alpha_{t_n}} - \frac{\sigma_{t_n}}{\alpha_{t_n}}\epsilon_{\theta}(x_{t_n}, t_n) + \frac{\sigma_{t_{n+1}}}{\alpha_{t_{n+1}}}(\epsilon_{\theta}(x_{t_n}, t_n) - \epsilon_{\theta}(x_{t_n \rightarrow t_{n+1}}, t_{n+1}))) - \frac{O(h^2)}{\alpha_{t_{n+1}}} \\
&= \frac{\sigma_{t_{n+1}}}{\alpha_{t_{n+1}}}(\epsilon_{\theta}(x_{t_n \rightarrow t_{n+1}}, t_{n+1}) - \epsilon_{\theta}(x_{t_n}, t_n)) - \frac{O(h^2)}{\alpha_{t_{n+1}}}
\end{aligned} \tag{14}$$

Finally, term 2 can be simplified as followed:

$$c_{out}(t_n)[F_{\theta}(x_{t_n}, t_n) - F_{\theta}(x_{t_n \rightarrow t_{n+1}}, t_{n+1})] = c_{out}(t_n)\frac{\sigma_{t_{n+1}}}{\alpha_{t_{n+1}}}(\epsilon_{\theta}(x_{t_n \rightarrow t_{n+1}}, t_{n+1}) - \epsilon_{\theta}(x_{t_n}, t_n)) - \frac{O(h^2)}{\alpha_{t_{n+1}}} \tag{15}$$

term 3:

$$\begin{aligned}
[c_{out}(t_n) - c_{out}(t_{n+1})]F_\theta(x_{t_n \rightarrow t_{n+1}}, t_{n+1}) &= [c_{out}(t_n) - c_{out}(t_{n+1})] \left(\frac{x_{t_n \rightarrow t_{n+1}} - \sigma_{t_{n+1}} \epsilon_\theta(x_{t_n \rightarrow t_{n+1}}, t_{n+1})}{\alpha_{t_{n+1}}} \right) \\
&\stackrel{(i)}{=} [c_{out}(t_n) - c_{out}(t_{n+1})] \left(\frac{x_{t_n} - \sigma_{t_n} \epsilon_\theta(x_{t_n}, t_n)}{\alpha_{t_n}} \right) \\
&\quad + [c_{out}(t_n) - c_{out}(t_{n+1})] \left(\frac{\sigma_{t_{n+1}}}{\alpha_{t_{n+1}}} (\epsilon_\theta(x_{t_n}, t_n) - \epsilon_\theta(x_{t_n \rightarrow t_{n+1}}, t_{n+1})) \right) \\
&= [c_{out}(t_n) - c_{out}(t_{n+1})] x_\pi \\
&\quad + [c_{out}(t_n) - c_{out}(t_{n+1})] \left(\frac{\sigma_{t_n}}{\alpha_{t_n}} (\epsilon - \epsilon_\theta(x_{t_n}, t_n)) \right) \\
&\quad + [c_{out}(t_n) - c_{out}(t_{n+1})] \left(\frac{\sigma_{t_{n+1}}}{\alpha_{t_{n+1}}} (\epsilon_\theta(x_{t_n}, t_n) - \epsilon_\theta(x_{t_n \rightarrow t_{n+1}}, t_{n+1})) \right)
\end{aligned} \tag{16}$$

where (i) hold according to the DPM-solver.

In our setting, the time interval is 100 and $t \geq 30$. Therefore, $|c_{out}(t_n) - c_{out}(t_{n+1})| \leq 10^{-7}$. However, in early stage, $\frac{\sigma_{t_n}}{\alpha_{t_n}} \geq 1$ and $[c_{out}(t_n) - c_{out}(t_{n+1})] \left(\frac{\sigma_{t_n}}{\alpha_{t_n}} \right)$ cannot be neglected. As number of iterations increases, the time t will gradually decrease, and $\frac{\sigma_{t_n}}{\alpha_{t_n}} < 1$. At this point, $[c_{out}(t_n) - c_{out}(t_{n+1})] \left(\frac{\sigma_{t_n}}{\alpha_{t_n}} \right)$ can be neglected. Then, term 3 can be formula as:

$$\begin{aligned}
[c_{out}(t_n) - c_{out}(t_{n+1})]F_\theta(x_{t_n \rightarrow t_{n+1}}, t_{n+1}) &= m + [c_{out}(t_n) - c_{out}(t_{n+1})] \left(\frac{\sigma_{t_n}}{\alpha_{t_n}} (\epsilon - \epsilon_\theta(x_{t_n}, t_n)) \right) \\
&\quad + [c_{out}(t_n) - c_{out}(t_{n+1})] \left(\frac{\sigma_{t_{n+1}}}{\alpha_{t_{n+1}}} (\epsilon_\theta(x_{t_n}, t_n) - \epsilon_\theta(x_{t_n \rightarrow t_{n+1}}, t_{n+1})) \right)
\end{aligned} \tag{17}$$

Finally, combining the results from term 1, term 2, and term 3, we obtain our CTS loss:

$$\begin{aligned}
L_{CD} &= \|f_\theta(x_{t_n}, t_n) - f_\theta(x_{t_n \rightarrow t_{n+1}}, t_{n+1})\|_2^2 \\
&= \|m + c_{skip}(t_{n+1})O((\Delta t)^{p+1}) \\
&\quad + c_{out}(t_n) \frac{\sigma_{t_{n+1}}}{\alpha_{t_{n+1}}} (\epsilon_\theta(x_{t_n \rightarrow t_{n+1}}, t_{n+1}) - \epsilon_\theta(x_{t_n}, t_n)) - \frac{O(h^2)}{\alpha_{t_{n+1}}} \\
&\quad + m + [c_{out}(t_n) - c_{out}(t_{n+1})] \left(\frac{\sigma_{t_n}}{\alpha_{t_n}} (\epsilon - \epsilon_\theta(x_{t_n}, t_n)) \right) \\
&\quad + [c_{out}(t_n) - c_{out}(t_{n+1})] \left(\frac{\sigma_{t_{n+1}}}{\alpha_{t_{n+1}}} (\epsilon_\theta(x_{t_n}, t_n) - \epsilon_\theta(x_{t_n \rightarrow t_{n+1}}, t_{n+1})) \right)\|_2^2 \\
&\stackrel{(ii)}{=} \|c_{out}(t_{n+1}) \left(\frac{\sigma_{t_{n+1}}}{\alpha_{t_{n+1}}} (\epsilon_\theta(x_{t_n \rightarrow t_{n+1}}, t_{n+1}) - \epsilon_\theta(x_{t_n}, t_n)) \right)\|_2^2 + \| [c_{out}(t_{n+1}) - c_{out}(t_n)] \left(\frac{\sigma_{t_n}}{\alpha_{t_n}} (\epsilon_\theta(x_{t_n}, t_n) - \epsilon) \right)\|_2^2 \\
&\quad - \frac{O(h^2)}{\alpha_{t_{n+1}}} + c_{skip}(t_{n+1})O((\Delta t)^{p+1}) + m \\
&= L_{CTS} - \frac{O(h^2)}{\alpha_{t_{n+1}}} + c_{skip}(t_{n+1})O((\Delta t)^{p+1}) + m
\end{aligned} \tag{18}$$

where (ii) is because we follow DreamFusionPoole et al. [2022] and omit the U-Net Jacobian term in practice. $\frac{\sigma_{t_n}}{\alpha_{t_n}} > 1$ in early stage, we can not omit the second term.

Therefore, we obtain two conclusions:

- L_{CTS} can be expressed as the sum the L_{CD} and two infinitesimal components, along with a term whose magnitude is bounded by 10^{-7} .

$$L_{CD} = L_{CTS} + \underbrace{\left(-\frac{O(h^2)}{\alpha_{t_{n+1}}}\right) + c_{skip}(t_{n+1})O((\Delta t)^{p+1})}_{\text{infinitesimal components}} + \underbrace{m}_{|m| \leq 10^{-7}} \quad (19)$$

$$h = \log\left(\frac{\alpha_{t_n}}{\sigma_{t_n}}\right) - \log\left(\frac{\alpha_{t_{n+1}}}{\sigma_{t_{n+1}}}\right)$$

- L_{CTS} can formula as:

$$L_{CTS} = \|w_1(\epsilon_\theta(x_{t_n \rightarrow t_{n+1}}, t_{n+1}) - \epsilon_\theta(x_{t_n}, t_n))\|_2^2 + \|w_2(\epsilon_\theta(x_{t_n}, t_n) - \epsilon)\|_2^2$$

$$w_1 = c_{out}(t_{n+1})\left(\frac{\sigma_{t_{n+1}}}{\alpha_{t_{n+1}}}\right) \quad (20)$$

$$w_2 = [c_{out}(t_{n+1}) - c_{out}(t_n)]\left(\frac{\sigma_{t_n}}{\alpha_{t_n}}\right)$$

The proof is completed.

Theorem 4 Assume that the pre-trained noise predictor $\epsilon_\theta(\cdot; \cdot)$ satisfies the Lipschitz condition. Define $\Delta := \sup|t_1 - t_2|$. For any given camera pose π , if convergence is achieved according to L_{CTS} , then there exists a corresponding real image $x_0 \sim p_{data}(x)$ such that:

$$\|x_\pi - x_0\|_2 = O(\Delta) \quad (21)$$

where $x_\pi = g(\theta, \pi)$ denotes the rendered image for pose π .

We offer two ways of proof. For the **Proof 1**, we directly utilize the CTS loss. For the **Proof 2**, we make use of Theorem 3.

Proof 1:

Proof Given $L_{CTS}(\xi) = 0$, for any t, s , we have $\epsilon(x_{s \rightarrow t}, t) = \epsilon_\theta(x_s, s)$ and $T \geq t_n \geq t_{n-1} \geq 0$. Assume G is DPM solver and follow the first-order definition of DPM-Solver, given e , we have:

$$\begin{aligned} G(x_{s \rightarrow t}, t, e) &= \frac{\alpha_e}{\alpha_t} x_{s \rightarrow t} - \sigma_e(e^{-h} - 1)\epsilon_\theta(x_{s \rightarrow t}, t) \\ &= \frac{\alpha_e}{\alpha_t} x_{s \rightarrow t} - \alpha_e \left(\frac{\sigma_t}{\alpha_t} - \frac{\sigma_e}{\alpha_e} \right) \epsilon_\theta(x_{s \rightarrow t}, t) \\ &= \alpha_e \frac{x_{s \rightarrow t} - \sigma_t \epsilon_\theta(x_{s \rightarrow t}, t)}{\alpha_t} + \sigma_e \epsilon_\theta(x_{s \rightarrow t}, t) \\ &= \alpha_e \frac{\alpha_t \left(\frac{x_s - \sigma_s \epsilon_\theta(x_s, s)}{\alpha_s} \right) + \sigma_t \epsilon_\theta(x_s, s) - \sigma_t \epsilon_\theta(x_{s \rightarrow t}, t) + O(h^2)}{\alpha_t} + \sigma_e \epsilon_\theta(x_{s \rightarrow t}, t) \\ &\stackrel{(iii)}{=} \alpha_e \left(\frac{x_s - \sigma_s \epsilon_\theta(x_s, s)}{\alpha_s} \right) + \sigma_e \epsilon_\theta(x_s, s) + L_1 O(h^2) \\ &= G(x_s, s, e) + L_1 O(h^2) \end{aligned} \quad (22)$$

where (iii) hold according to the $\epsilon_\theta(x_{s \rightarrow t}, t) = \epsilon_\theta(x_s, s)$. When we set $e = 0$, the $G(x_s, s, 0)$ can be treated as diffusion model D that directly predicts the original image x_0 . We define $D(x_s, s) = G(x_s, s, 0)$ and $D(x_{s \rightarrow t}, t) = D(x_s, s) + L_1 O(h^2)$.

Let e_n represent the error at t_n , which is defined as:

$$e_n := D(x_{t_n}, t_n) - x_0. \quad (23)$$

We can derive the error at t_{n+1} given the error at t_n :

$$\begin{aligned}
e_n &= D(x_{t_n}, t_n) - x_0 \\
&= D(x_{t_n}, t_n) - D(x_{t_{n-1} \rightarrow t_n}, t_n) + D(x_{t_{n-1} \rightarrow t_n}, t_n) - x_0 \\
&= \frac{x_{t_n} - \sigma_{t_n} \epsilon_\theta(x_{t_n}, t_n)}{\alpha_{t_n}} - \frac{x_{t_{n-1} \rightarrow t_n} - \sigma_{t_n} \epsilon_\theta(x_{t_{n-1} \rightarrow t_n}, t_n)}{\alpha_{t_n}} \\
&\quad + D(x_{t_{n-1}}, t_{n-1}) - x_0 + L_1 O((t_n - t_{n-1})^2) \\
&= \frac{1}{\alpha_{t_n}} (x_{t_n} - x_{t_{n-1} \rightarrow t_n}) + \frac{\sigma_{t_n}}{\alpha_{t_n}} (\epsilon_\theta(x_{t_{n-1} \rightarrow t_n}, t_n) - \epsilon_\theta(x_{t_n}, t_n)) + e_{n-1} + L_1 O((t_n - t_{n-1})^2)
\end{aligned} \tag{24}$$

According to the Lipschitz condition, we can further derive:

$$\begin{aligned}
\|e_n\| &\leq \frac{1}{\alpha_{t_n}} \|x_{t_n} - x_{t_{n-1} \rightarrow t_n}\| + \frac{\sigma_{t_n}}{\alpha_{t_n}} \|\epsilon_\theta(x_{t_{n-1} \rightarrow t_n}, t_n) - \epsilon_\theta(x_{t_n}, t_n)\| + \|e_{n-1}\| + L_1 O((t_n - t_{n-1})^2) \\
&\stackrel{(iv)}{\leq} \frac{1}{\alpha_{t_n}} O((t_n - t_{n-1})^2) + \frac{\sigma_{t_n}}{\alpha_{t_n}} L \|x_{t_{n-1} \rightarrow t_n} - x_{t_n}\| + \|e_{n-1}\| + L_1 O((t_n - t_{n-1})^2) \\
&\stackrel{(v)}{\leq} \|e_{n-1}\| + K O((t_n - t_{n-1})^2)
\end{aligned} \tag{25}$$

where (iv), (v) hold according to the local error of Euler solver and Lipschitz condition of ϵ_θ . Therefore, we can derive the error recursively:

$$\begin{aligned}
\|e_T\| &\leq K \sum_{i=1}^{N-1} O((t_i - t_{i-1})^2) \\
&\leq K \sum_{i=1}^{N-1} (t_i - t_{i-1}) O(\Delta) \\
&\leq K O(\Delta) (T - \xi)
\end{aligned} \tag{26}$$

This shows that CTS is capable of achieving the same accuracy as multi-step approaches in a single-step generative frame work, thus demonstrating its efficiency and broad applicability for optimization-based generation. The proof is completed.

Proof 2:

Proof According to theorem 3 and CMSong et al. [2023], the CTS loss is equivalent to consistency loss and the consistency function satisfies the Lipschitz condition. Given $L_{CTS}(\xi) = 0$, we have $L_{CD}(\xi) \leq O((\Delta t)^2)$ and $f_\theta(x_{s \rightarrow t}, t) \leq f_\theta(x_s, s) + O((\Delta t)^2)$. And $T \geq t_n \geq t_{n-1} \geq 0$.

$$\begin{aligned}
e_n &= f_\theta(x_{t_n}, t_n) - x_0 \\
&= f_\theta(x_{t_n}, t_n) - f_\theta(x_{t_{n-1} \rightarrow x_n}, t_n) + f_\theta(x_{t_{n-1} \rightarrow x_n}, t_n) - x_0 \\
&\leq f_\theta(x_{t_n}, t_n) - f_\theta(x_{t_{n-1} \rightarrow x_n}, t_n) + f_\theta(x_{t_{n-1}}, t_{n-1}) - x_0 + O((\Delta t)^2)
\end{aligned} \tag{27}$$

According to the Lipschitz condition, we can further derive:

$$\begin{aligned}
\|e_n\| &\leq \|f_\theta(x_{t_n}, t_n) - f_\theta(x_{t_{n-1} \rightarrow x_n}, t_n)\| + \|e_{n-1}\| + O((\Delta t)^2) \\
&\stackrel{(vi)}{\leq} L \|x_{t_n} - x_{t_{n-1} \rightarrow x_n}\| + \|e_{n-1}\| + O((\Delta t)^2) \\
&\stackrel{(vii)}{\leq} L (O(t_n - t_{n+1})^2) + \|e_{n-1}\| + O((\Delta t)^2) \\
&\leq (L + 1) O((t_n - t_{n+1})^2) + \|e_{n-1}\| \\
&= \|e_{n-1}\| + O((t_n - t_{n+1})^2)
\end{aligned} \tag{28}$$

where (vi) and (vii) hold according to the Lipschitz condition and local error of Euler solver respectively. Therefor, we can drive the error recursively:

$$\begin{aligned}
||e_T|| &\leq \sum_{i=1}^{N-1} O((t_i - t_{i-1})^2) \\
&\leq \sum_{i=1}^{N-1} (t_i - t_{i-1})O((\Delta)) \\
&\leq O((\Delta))(T - \xi)
\end{aligned} \tag{29}$$

The proof is completed.

Corollary 1 Based on Theorem. 3, we can derive two conclusions:

- Existing methodsZhong et al. [2024], Chen et al. [2024b] which incorporate Latent Consistency Model for 3D generation can be amalgamated into our framework.
- Consistency functionSong et al. [2023] can ensures both self-consistency and cross-consistency.

Consistent3DWu et al. [2024b] and CCDLi et al. [2024b] drive the inspiration from Consistency modelSong et al. [2023], however, they are still trained based on Stable Diffusion-2-1Ho et al. [2020]. Hence, we merely consider DreamLCMZhong et al. [2024] and VividdreamerChen et al. [2024b] that based on LCMLuo et al. [2023].

Proof DreamLCMZhong et al. [2024]:

$$L_{DreamLCM} = \mathbb{E}_{t,c}[w(t)(\epsilon_\theta(x_t, t) - \epsilon) \frac{\partial g(\theta, c)}{\partial \theta}] \tag{30}$$

where x_t is obtained by Euler Solver from x_s and $x_s = \alpha_s x_\pi + \sigma_s \epsilon$, $\epsilon \in N(0, I)$.

VividreamerChen et al. [2024b]:

$$L_{vividreamer} = \mathbb{E}_{t,c}[||w(t)(x_\pi - f(x_s, s))||_2^2] \tag{31}$$

where $x_s = \alpha_s x_\pi + \sigma_s \epsilon$.

For DreamLCMZhong et al. [2024], according to eq. 18, L_{CD} can express as:

$$\begin{aligned}
L_{CD} &= ||f_\theta(x_{t_n}, t_n) - f_\theta(x_{t_n \rightarrow t_{n+1}}, t_{n+1})||_2^2 \\
&= ||m + c_{skip}(t_{n+1})O((\Delta t)^{p+1}) \\
&\quad + c_{out}(t_n) \frac{\sigma_{t_{n+1}}}{\alpha_{t_{n+1}}} (\epsilon_\theta(x_{t_n \rightarrow t_{n+1}, t_{n+1}}) - \epsilon_\theta(x_{t_n}, t_n)) - \frac{O(h^2)}{\alpha_{t_{n+1}}} \\
&\quad + m + [c_{out}(t_n) - c_{out}(t_{n+1})] \left(\frac{\sigma_{t_n}}{\alpha_{t_n}} \right) (\epsilon - \epsilon_\theta(x_{t_n}, t_n)) \\
&\quad + [c_{out}(t_n) - c_{out}(t_{n+1})] \left(\frac{\sigma_{t_{n+1}}}{\alpha_{t_{n+1}}} (\epsilon_\theta(x_{t_n}, t_n) - \epsilon_\theta(x_{t_n \rightarrow t_{n+1}}, t_{n+1})) \right)||_2^2 \\
&= ||m + c_{skip}(t_{n+1})O((\Delta t)^{p+1}) \\
&\quad + c_{out}(t_{n+1}) \frac{\sigma_{t_{n+1}}}{\alpha_{t_{n+1}}} (\epsilon_\theta(x_{t_n \rightarrow t_{n+1}, t_{n+1}}) - \epsilon_\theta(x_{t_n}, t_n)) - \frac{O(h^2)}{\alpha_{t_{n+1}}} \\
&\quad + m + [c_{out}(t_n) - c_{out}(t_{n+1})] \left(\frac{\sigma_{t_n}}{\alpha_{t_n}} \right) (\epsilon - \epsilon_\theta(x_{t_n \rightarrow t_{n+1}, t_{n+1}}) + \epsilon_\theta(x_{t_n \rightarrow t_{n+1}, t_{n+1}}) - \epsilon_\theta(x_{t_n}, t_n))||_2^2 \\
&= m + c_{skip}(t_{n+1})O((\Delta t)^{p+1}) \\
&\quad + [c_{out}(t_{n+1}) \frac{\sigma_{t_{n+1}}}{\alpha_{t_{n+1}}} + [c_{out}(t_n) - c_{out}(t_{n+1})] \left(\frac{\sigma_{t_n}}{\alpha_{t_n}} \right)] (\epsilon_\theta(x_{t_n \rightarrow t_{n+1}, t_{n+1}}) - \epsilon_\theta(x_{t_n}, t_n)) \\
&\quad + [c_{out}(t_n) - c_{out}(t_{n+1})] \left(\frac{\sigma_{t_n}}{\alpha_{t_n}} \right) \underbrace{(\epsilon - \epsilon_\theta(x_{t_n \rightarrow t_{n+1}, t_{n+1}}))}_{\text{loss of DreamLCM}}
\end{aligned} \tag{32}$$

DreamLCM assumes that the denoising process of LCM follows a smooth PF-ODE trajectory with a small slope. This assumption allows us to omit the term of $(\epsilon_\theta(x_{t_n \rightarrow t_{n+1}}, t_{n+1}) - \epsilon_\theta(x_{t_n}, t_n))$, therefore, in this assumption, L_{DreamLCM} is a special case of L_{CTS} .

For VividdreamerChen et al. [2024b], we have:

$$\begin{aligned}
L_{\text{vividdreamer}} &= \|x_\pi - f(x_s, s)\|_2^2 \\
&= \|x_\pi - (c_{\text{in}}(s)x_\pi + c_{\text{skip}}(s)\frac{x_s - \sigma_s \epsilon_\theta(x_s, s)}{\alpha_s})\|_2^2 \\
&= \|(1 - c_{\text{skip}}(s))x_\pi - c_{\text{in}}x_s + c_{\text{skip}}(s)x_\pi - c_{\text{skip}}(s)\frac{x_s - \sigma_s \epsilon_\theta(x_s, s)}{\alpha_s}\|_2^2 \\
&= \|(1 - c_{\text{skip}}(s))x_\pi - c_{\text{in}}(\alpha_s x_\pi + \sigma_s \epsilon) + c_{\text{skip}}(s)\frac{\alpha_s x_\pi - \alpha_s x_\pi - \sigma_s(\epsilon - \epsilon_\theta(x_s, s))}{\alpha_s}\|_2^2 \\
&= \|(1 - c_{\text{skip}}(s))x_\pi - c_{\text{in}}(s)(\alpha_s x_\pi + \sigma_s \epsilon) + c_{\text{skip}}(s)\frac{\sigma_s}{\alpha_s}(\epsilon - \epsilon_\theta(x_s, s))\|_2^2 \\
&= \|[1 - c_{\text{skip}}(s) - c_{\text{in}}(s)\alpha_s]x_\pi - c_{\text{in}}(s)\sigma_s \epsilon + c_{\text{skip}}(s)\frac{\sigma_s}{\alpha_s}(\epsilon - \epsilon_\theta(x_s, s))\|_2^2 \\
&\stackrel{(viii)}{\approx} c_{\text{skip}}(s)\frac{\sigma_s}{\alpha_s}(\epsilon - \epsilon_\theta(x_s, s))\|_2^2
\end{aligned} \tag{33}$$

where (viii) hold according to the $c_{\text{skip}}(s) + c_{\text{in}}(s) \approx 1$ and $\mathbb{E}[\epsilon] = 0$. Therefore, Vividdreamer is a special case of our CTS loss.

According to the definition of self-consistency and cross-consistency(SDS) in previous methodsWu et al. [2024b], Li et al. [2024b], we can observe that L_{CTS} simultaneously ensures two types of consistency:

$$\begin{aligned}
L_{\text{CTS}} &= \|c_{\text{out}}(t_{n+1})\left(\frac{\sigma_{t_{n+1}}}{\alpha_{t_{n+1}}}(\epsilon_\theta(x_{t_n \rightarrow t_{n+1}}, t_{n+1}) - \epsilon_\theta(x_{t_n}, t_n))\right)\|_2^2 \\
&\quad \underbrace{\hspace{10em}}_{\text{self-consistency term}} \\
&\quad + \|[c_{\text{out}}(t_{n+1}) - c_{\text{out}}(t_n)]\left(\frac{\sigma_{t_n}}{\alpha_{t_n}}(\epsilon_\theta(x_{t_n}, t_n) - \epsilon)\right)\|_2^2 \\
&\quad \underbrace{\hspace{10em}}_{\text{cross-consistency term(SDS loss)}}
\end{aligned} \tag{34}$$

The proof is complete.

7.1.2 Ablation Study for m

It is worth noting that our generation process exhibits inherent randomness, meaning identical prompts may not consistently produce the exact same objects or scenes. Therefore, we primarily compare the overall texture trends and fine details. Next, we conduct ablation studies on m separately for objects and scenes synthesis. The experimental results demonstrate that the m has negligible impact on the results, whether synthesizing objects or scenes.

Scenes As shown in Figure 10. Despite slight color differences, the general texture patterns and detailed features are identical.

Objects As shown in Figure 9, the overall shape and fine details of the objects remain consistent.

7.2 Pipeline

Due to space limitations in the regular paper, we omit detailed descriptions of certain technical implementations. In this section, we provide a comprehensive account of our contributions and present the overall pipeline in detail.

Our Contributions for Indoor Scene Generation:

- Layout Generation:



Figure 9: Ablation Study of m in Object Generation.

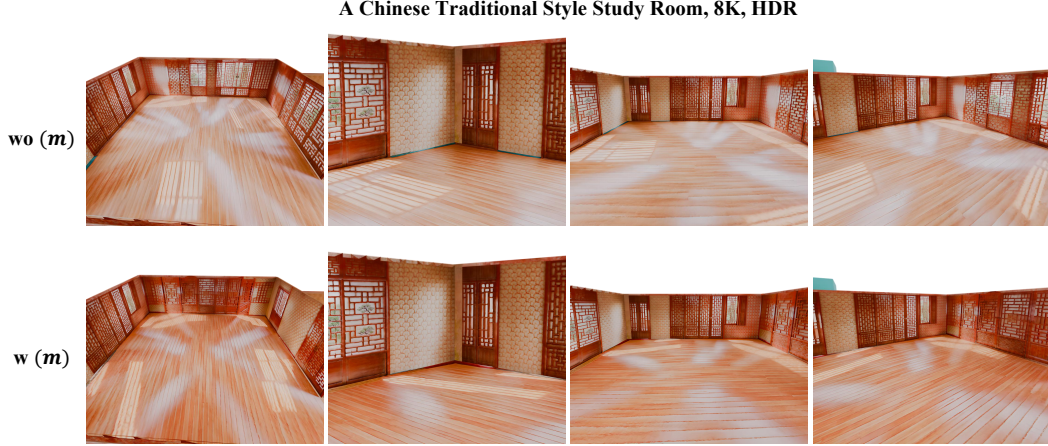


Figure 10: Ablation Study of m in Scene Generation. After training, we distill the texture field into a texture map and import the environment into BlenderCommunity [2018] for visualization.

- **Interactive Programmatic Verification Mechanism:** Ensure that no overlapping occurs between furniture.
- **Cluster-based Orientation Assignment Strategy:** Ensure accuracy orientation generation.
- Object Generation:
 - **Consistency Trajectory Sampling(CTS):** Realistic furniture generation.
 - **CTS without noise:** Efficiently generating furniture.
 - **theorem analysis:** 2 theorem and 1 corollary.
- Environment Optimization:
 - **multi-resolution texture field and normal-aware decoder:** high-resolution, style consistency, and rich texture generation
 - **Optimization via CTS without noise:** Realistic texture generation
 - **zigzag adaptive camera trajectory:** Multi-scale Scene Generation
 - **several techniques:** Improve numerical stability
- Physical edition: Integrate physical simulation to ensure the physical plausible editing. We propose two way to perform physical plausible editing.
 - **Employing bounding boxes as proxies to conduct physics-based simulations.**
 - **Extracting meshes as proxies for performing physics-based simulations.**

Next, we present a detailed account of our contributions.

7.2.1 Layout Generation

Layout Generation consists of four key functions as shown in Figure 11:

- User offers a description of the house.
- LLM converts the textural description into 3D layout.
 - At this point, it already contains initial layout information, including the floorplan, descriptions, positions, and scales of furniture.
 - However, the initial layout is typically obtained through a single query to the LLM, which often results in overlapping furniture placements.
 - Next, Iterative Programmatic Verification Mechanism is proposed to address overlapping.
- Iterative Programmatic Verification Mechanism
 - Convert the 3D layout into programs and execute it to check for conflicts.

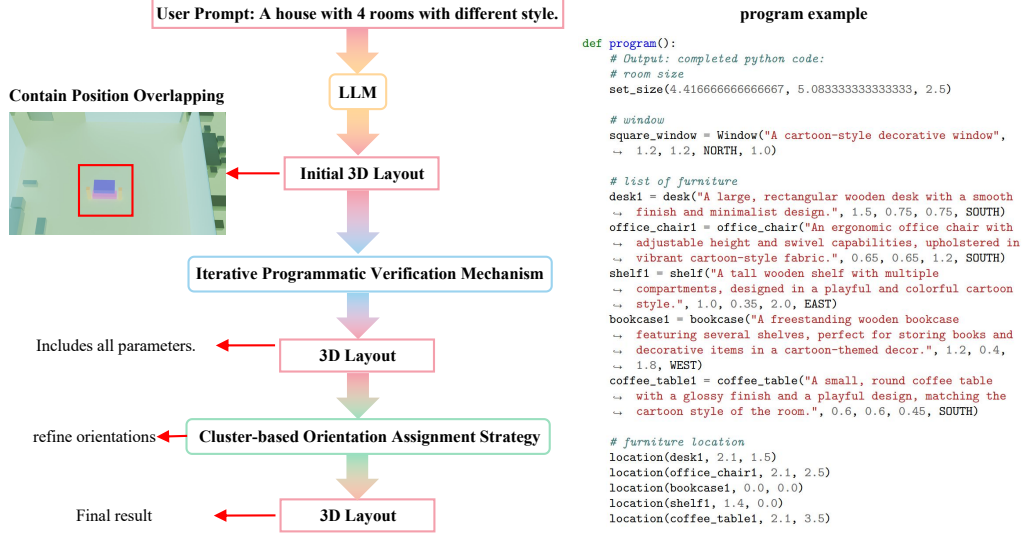


Figure 11: Layout pipeline and code example.

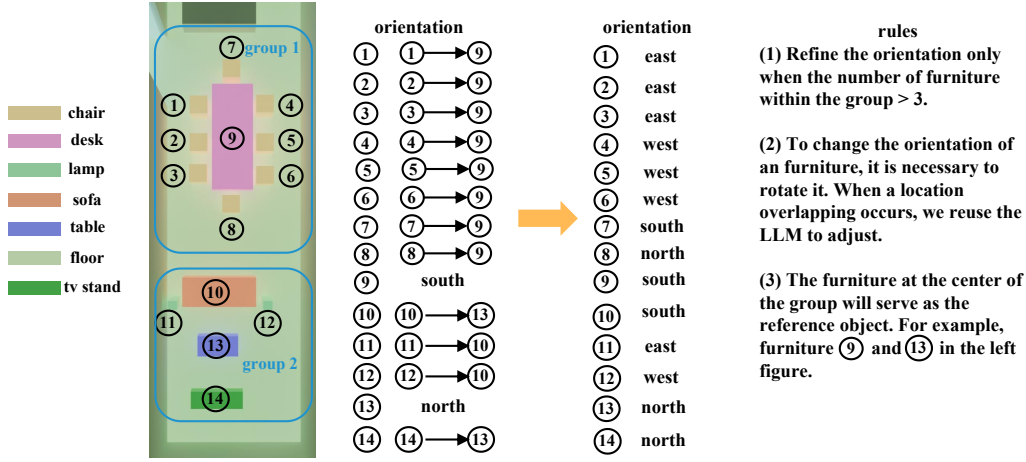


Figure 12: Cluster-based Orientation Assignment.

- Iteratively feed the error and program into the LLM for parameter refinement.
- The previous methodsFu et al. [2024], Yang et al. [2024b] generate all the layout parameters in a single query to the LLM. However, when dealing with complex scenes containing numerous furniture, the LLM often struggles to account for all inter-furniture relationships, and it is challenging to generate accurate orientations through a single query.
- Next, Cluster-based Orientation Assignment is proposed to generate accuracy orientation.
- Cluster-based Orientation Assignment Strategy
 - We first partition the furniture into several groups.
 - Within each group, object orientations are determined not by cardinal directions, but through inter-object spatial relations. In this way, LLM is only required to account for spatial relationships within the current group of furniture.
 - As shown in Figure 12, we first select a reference object from within the group to prevent circular argument. Then we generate the orientation of each furniture relative to the others, and finally convert it into cardinal directions.
- Convert final program to 3D layout.

Our framework can generate more furniture with accurate spatial orientations. **On average, a single room contains approximately 8 pieces of furniture, while a house with 4 rooms averages around 40 pieces.** In Sec. 7.6 and Sec. 7.5, we will compare our method with other approaches and conduct ablation studies to demonstrate its superiority.

7.2.2 Object Generation

Motivation. Following Consistent3DWu et al. [2024b], given a ODE sampling process for a 3D model θ :

$$d\theta = -\dot{\sigma}_t \sigma_t \nabla \log p_t(\theta) dt, \quad (35)$$

where θ is randomly initialized according to a certain distribution. And Following DreamFusionPoole et al. [2022] and SJCWang et al. [2023a], the 3D score function $\nabla_\theta \log p_t(\theta)$ from the 2D score function using the chain rule:

$$\nabla_\theta \log p_t(\theta) = \mathbb{E}_\pi[\nabla_{x_\pi} \log p_t(x_\pi) \frac{\partial x_\pi}{\partial \theta}], \quad (36)$$

where the x_π is rendered image, and the 2D score function $\nabla_x \log p_t(x)$ can be estimated as $\nabla_x \log p_t(x) = \frac{D_\phi(x, t) - x}{\sigma_t^2}$ by a pre-trained diffusion model $D_\phi(x, t)$. Therefore, the key to generating a satisfactory 3D model is to accurately perform the 3D ODE sampling in Eq. 36 using the pre-trained diffusion model. Consistent3DWu et al. [2024b] proposes Consistency Distillation Sampling(CDS) loss to distilling the deterministic prior into the 3D model:

$$\mathbb{E}_\pi[\lambda(t) \|D_\phi(x_t, t, y) - sg(D_\phi(x_{t \rightarrow s}, s, y))\|_2^2], \quad (37)$$

where $sg(\cdot)$ is a stop-gradient operator, $t > s$. They believe that less-noisy sample lies on the 3D model's target ODE trajectory, and are used to guide more-noisy sample. CCDLi et al. [2024b] builds upon Consistent3D by introducing Conditional Guidance loss and Compact Consistency loss to enhance the consistency. CCD follows Consistent3D and still treats less-noisy sample as golden to guide the more-noisy sample(The stop-gradient operator is not mentioned in the CCD paper, but it is implemented in the CCD code: <https://github.com/LMozart/ECCV2024-GCS-BEG.git>). However, less-noisy samples may not necessarily lie on the target ODE trajectory. Treating these as golden for guiding more-noisy samples could introduce artifacts and inconsistencies in the model. Another line of worksLi et al. [2024a], Liang et al. [2024] also improve the consistency and match two adjacent samples. DreamLCMZhong et al. [2024] and VividdreamerChen et al. [2024b] directly apply Consistency modelLuo et al. [2023] as based model for generating. However, the former is based on the smoothness assumption, while the latter employs a consistency modelLuo et al. [2023] as the based model to enhance the SDS lossPoole et al. [2022]. Therefore, these models only adopt the concept of consistency modelWu et al. [2024b], Li et al. [2024b] or employ the consistency model as based modelZhong et al. [2024], Chen et al. [2024b], but fail to conduct in-depth research on their interrelationships.

In contrast, our CTS loss directly originates from the consistency modelSong et al. [2023], is derived from the consistency functionSong et al. [2023], and explicitly reveals the relationship between the two.

Our CTS loss:

$$\begin{aligned} L_{CTS} &= \mathbb{E}[\|w_1(t)(\epsilon_\theta(x_{s \rightarrow t}, t, y) - \epsilon_\theta(x_s, s, \emptyset))\|_2^2 + \|w_2(s, t)(\epsilon_\theta(x_s, s, \emptyset) - \epsilon)\|_2^2] \\ w_1(t) &= c_{out}(t) \left(\frac{\sigma_t}{\alpha_t}\right) \\ w_2(s, t) &= [c_{out}(t) - c_{out}(s)] \left(\frac{\sigma_s}{\alpha_s}\right), \end{aligned} \quad (38)$$

We can also apply consistency lossSong et al. [2023]:

$$\mathbb{E}[\|f(x_s, s, y) - f(x_{s \rightarrow t}, t, y)\|_2^2] \quad (39)$$

However, this formulation is not conducive to integrating our method with other approachesHo and Salimans [2021], Armandpour et al. [2023] that act on the predicted noise $\epsilon_\theta(\cdot; \cdot)$. Our CTS loss effectively resolves these issues.

Algorithm. It is worth noting that $w_2(s, t)$ tends to zero as t decreases. Hence we remove the second term when $t \leq 500$. Additionally, we employ L_{scale} , L_{layout} , and L_{normal} for detail. Neither A nor B is our contribution; thus, we will not conduct ablation studies on them in the subsequent ablation experiments.

$$\begin{aligned}
L_{scale} &= \frac{1}{N} \sum_{i=1}^N \max(s_i) \\
L_{normal} &= \frac{1}{M} \sum_{i=1}^M w_i (1 - n_i^T \tilde{n}_i) \\
L_{Layout} &= d^x(G_x, x_i, h_i) + d^y(G_y, y_i, w_i) + d^z(G_z, z_i, l_i) \\
d^x(G_x, x_i, h_i) &= \|\min(G_x) - (x_i - \frac{h_i}{2})\|_2^2 + \|\max(G_x) - (x_i + \frac{h_i}{2})\|_2^2 \\
w_i &= \alpha_i \prod_{j=1}^i (1 - \alpha_j),
\end{aligned} \tag{40}$$

α_i is the pixel translucency determined by the opacity of the i -th Gaussian kernel and the pixel's position. $s_i \in \mathbb{R}^3$ is scale of i -th Gaussian. N is the number of Gaussian, M is the number of pixel. Different from Gala3D Zhou et al. [2024], while Gala3D restricts objects to lie strictly within bounding boxes, our L_{layout} optimizes for tight alignment with box boundaries, enabling direct physics simulation using the bounding boxes. For more clarity, we summarize our entire furniture generation procedure with the proposed CTS in Algorithm 1.

Algorithm 1 SceneLCM for Objects

Require: 3D model parameters θ , training iteration n , latent consistency model network ϕ denoising timestep from N_{min} to N_{max} , text prompt y , fixed noise ϵ , warm up timestep T_{warm_up} , warm up step N_{warm_up} , and timestep t_{cut} . DPM-Solver $G(\cdot; \cdot, \cdot)$

for $i = 1, 2, \dots, N$ **do**

$r = 1 - \min(i/N_{warm_up}, 1)$

$T_{min} \leftarrow \text{int}(N_{min} + r * N_{warm_up})$, $T_{max} \leftarrow \text{int}(N_{max} + r * N_{warm_up})$

camera pose c , $x_\pi = g(\theta, c)$

t sample from $[T_{min}, T_{max}]$

s sample from $[t - 2 * t_{cut}, t - t_{cut}]$ ▷ Obtain timestep s and t .

if $i \leq T_{warm_up}$ **then**

$x_s \leftarrow \alpha_s x_\pi + \sigma_s \epsilon$ ▷ add noise by DDPM.

else

$x_s \leftarrow x_\pi$

end if

$x_{s \rightarrow t} \leftarrow G(x_s; s, t)$ ▷ Obtain $x_{s \rightarrow t}$ by Euler Solver.

if $i \leq T_{warm_up}$ **then**

calculate CTS loss

$\nabla_\theta L_{CTS} \leftarrow w_2(s, t)(\epsilon_\phi(x_s, s, y) - \epsilon) \frac{\partial g(\theta, c)}{\partial \theta}$

else

$\nabla_\theta L_{CTS} \leftarrow 0$

end if

$\nabla_\theta L_{CTS} \leftarrow \nabla_\theta L_{CTS} + w_1(t)(\epsilon_\phi(x_t, t, y) - \epsilon_\phi(x_s, s, \emptyset)) \frac{\partial g(\theta, c)}{\partial \theta}$

$\theta \leftarrow \theta + \eta \nabla_\theta L_{CTS}$ ▷ Besides the CTS loss, we also have losses L_{scale} , L_{layout} , and L_{normal} , which are omitted here for simplicity.

end for

Noise Removal. The generation process progresses through two sequential stages over decreasing time t : semantic generation and detail generation. Once 3DGS developed distinct semantic signal which align with the text prompts, adding noise drives the model to alter details for text alignment. However, as most text lack high-frequency specific, e.g., "An iron man with white hair. 8K HDR", the focus should be on enhancing detail generation rather than forces alignment. Therefore, we eliminate

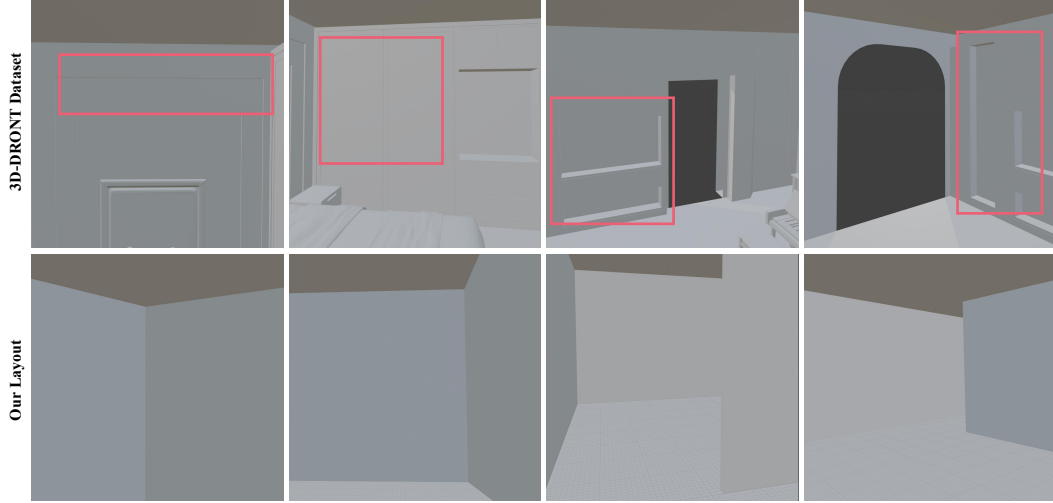


Figure 13: Comparisons of 3D layout mesh and scene mesh in 3D FRONT dataset. Our layout consists of simple planar structures. In contrast, intricate geometries on walls within 3D FRONT dataset.

the noise and set $x_s = x_\pi$ as shown in Algorithm 1, to allow the model to concentrate on detail generation and improve the training efficiency. In Sec. 7.6, we conduct ablation studies to verify both the generation efficiency and the visual details of the generated results.

Noise removal primarily impacts processing speed at the object level, but at the scene level, this technique becomes crucial and significantly affects the generation quality. We will verify this point in subsequent experiments.

7.2.3 Environment Generation

Five key components:

- Multi-resolution Texture Field
- Normal-aware Decoder
- Optimization via CTS loss
- Zigzag adaptive camera trajectory
- Several techniques

Multi-resolution Texture Field. Indoor scene texture generation methods can be categorized into two types: Inpaint-based methodsHuang et al. [2024b], Wang et al. [2024a] and Optimization-based methodsChen et al. [2024a]. Inpaint-based methods directly inpaint texture map frame by frame conditioned on depth map. However, the inpainting results are strictly constrained by the depth map, and most environments(3D FRONT) utilized by existing methodsHuang et al. [2024b], Wang et al. [2024a] contain complex geometric structures. As shown in Figure 13, due to the extreme flatness of our layout, inpaint-based methods applied to our scenes can only generate appearances with monotonous colors and missing textures. Optimization-based methods can address the aforementioned issues; however, due to gradient conflicts across different viewpoints, they often suffer from multi-view inconsistency.

Inspired by SceneTexChen et al. [2024a], we introduce multi-resolution texture field to encode appearance of environment. In particular, we encode texture features for all UV coordinate q at each scale, can concatenate those features as the output UV embedding $\varepsilon(q)$ to represent all texture details.

Normal-aware Cross-attention Decoder. Since the texture is optimized in image space, texture are often constrained by limited field of view and self-occlusion. As a result, the optimized texture often suffers from style inconsistency. SceneTexChen et al. [2024a] decodes rgb value by cross-attending to all pre-sampled anchors in current instance. While SceneTex ensures style consistency, it overlooks a

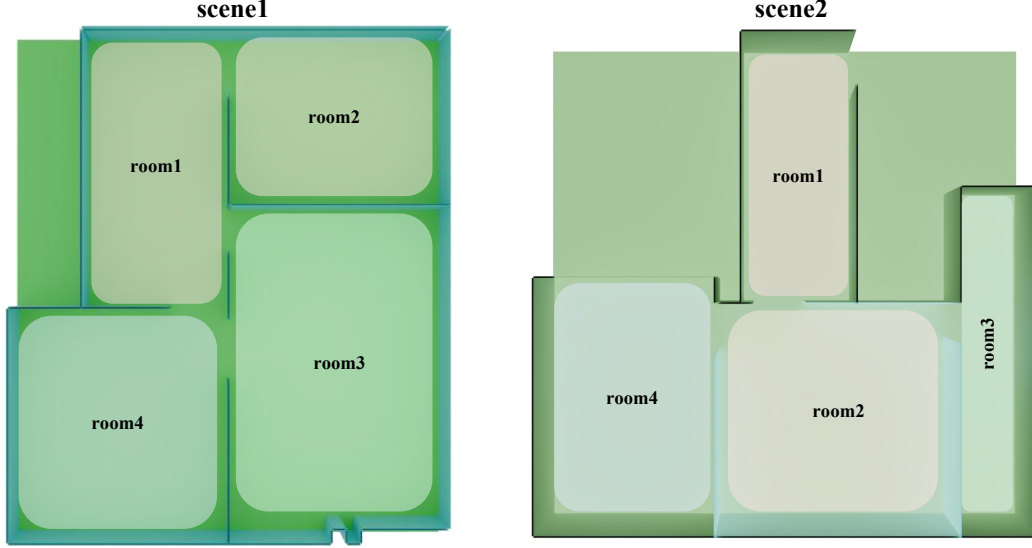


Figure 14: Room Scale. Our layout encompasses rooms of various scales, necessitating a camera trajectory that is sufficiently robust.

critical fact: regions with different normals often exhibit distinct texture characteristics. For example, the floor, walls, and ceiling of a room typically feature distinct styles.

Therefore, we decode rgb value by cross-attending to the pre-sampled anchors which have the same normal. This improvement introduces minimal stylistic variation while ensuring that regions with different normals retain their distinct texture characteristics. Sec. 7.6 conduct ablation study for normal-aware decoder.

Zigzag adaptive camera trajectory. As shown in Figure 14, Our layout includes rooms of different scales, requiring a robustly designed camera trajectory to cover all areas. Previous methods either require predefined camera trajectories Yang et al. [2024a], Chen et al. [2024a] or sphere camera trajectory(place the camera at the room’s center for rotation) Li et al. [2024a], Huang et al. [2024b], Wang et al. [2024a]. However, manually defining camera trajectories is inapplicable to scenes of all scales and requires substantial manual effort; moreover, sphere camera trajectory fails to accommodate all room with different scale as shown in Figure 15.

Therefore, we propose a zigzag adaptive camera trajectory that can accommodate indoor scenes of varying scales. As shown in Figure 16, the camera’s xy coordinates move in the opposite direction to those of the target, while its height is inversely proportional to the target’s height(z axis). Three advantages of zigzag camera trajectory:

- Maintaining a reasonable camera-target distance allows the diffusion model Ho et al. [2020] to recognize scene semantics (e.g., floor, walls, ceiling), enabling style differentiation for semantic instances.
- Ensures the angle between camera rays and target surface normals remains within acceptable limits.
- Camera view can cover more furniture and environment elements, avoiding texture missing.

We conducted generation tasks on a total of 17 rooms across 4 houses, validating the effectiveness of our proposed method.

Optimization via CTS loss. We apply our CTS loss and zigzag camera trajectory for scene optimization. Training schedule:

- warm up stage: we set the room center as the camera position. And randomly choose a furniture center as the target. Then we place all furniture into layout and render image. LCMLuo et al. [2023] used to optimize environment.

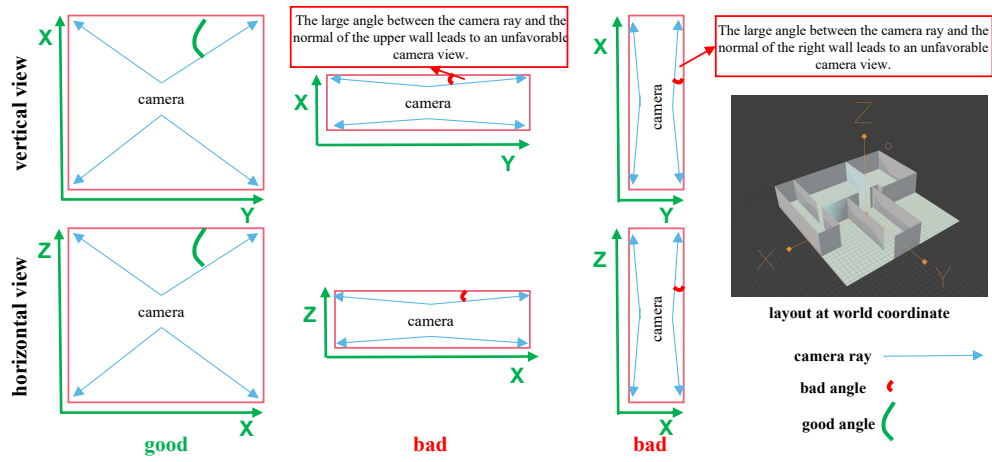


Figure 15: The issue of sphere camera trajectory. When the room has equal length and width, placing the camera at the center can capture a relatively good camera view (as shown on the left). However, when the room is relatively narrow (as shown on the right), the camera rays will deviate excessively from the environmental normals, resulting in an unfavorable viewing angle and lead to bad view.

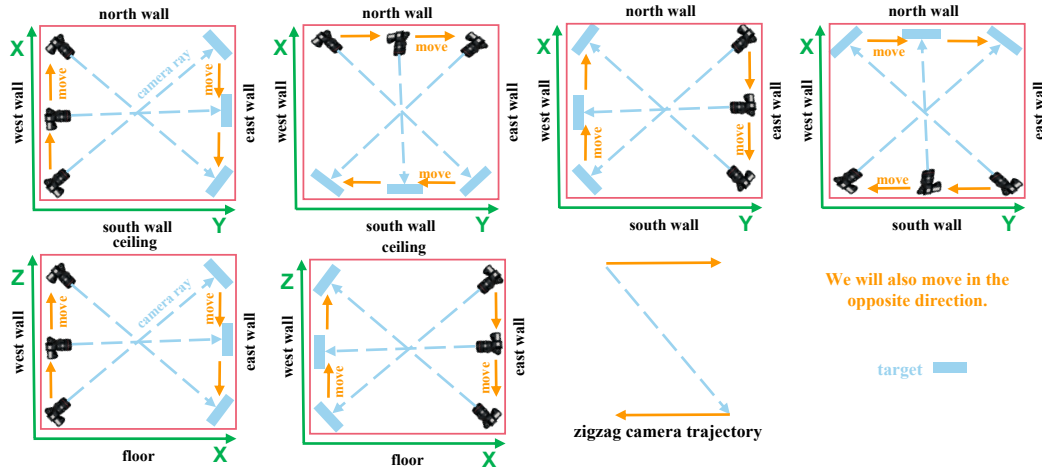


Figure 16: Zigzag camera trajectory. The first row is the camera trajectory viewed from the z-axis, the second row is the camera trajectory viewed from the y-axis. The camera moves along the wall, while the target moves in the opposite direction relative to the camera along the opposite wall. This approach offers three key advantages: (1) It prevents the short distance from causing diffusion models to fail in recognizing scene elements; (2) It ensures the angle between camera rays and target surface normals remains within acceptable limits; (3) It maximizes object coverage in the frame, avoiding texture monotony.

- object remove stage: we select half of the furniture from the furniture list to incorporate into the layout for rendering, while simultaneously sampling camera positions from the zigzag adaptive camera trajectory.
- noise removal stage: we remove the noise from CTS loss.

Our method not only synthesizes photorealistic appearance but also preserves fine-grained surface textures. Furthermore, it autonomously generates sophisticated wall decorations including windows, curtains, and lamps. The noise removal is critical for environment optimization. And we conduct the ablation study in Sec. 7.6.

Several techniques We conduct ablation study in Sec. 7.6.

7.2.4 Physical Editing

We provide two way to perform physically plausible editing.

- Thanks to the L_{layout} constraint, our furniture is strictly confined within bounding boxes and tightly aligned with their edges. This enables direct utilization of the bounding boxes for physics-based simulation. We use the bounding box as proxy and = perform the physical simulation in blenderCommunity [2018] and export the translation and rotation matrix.
- For more precise physics simulation, we employ RadeGSZhang et al. [2024a] to extract the mesh, which is then utilized as a proxy for conducting the physical simulation.

7.3 Discussion for Related Work

7.3.1 Indoor Scene Generation

There are some related works, we will explain the reasons for comparing or not comparing them.:

- Generative Framework: only require a pre-trained diffusion model ‘
 - Text2NerfZhang et al. [2024b] and Text2RoomHöllein et al. [2023]: both of them are inpaint methods. We compare one of them.
 - set-the-sceneCohen-Bar et al. [2023]: we follow the official guidelines and create the same layout for training. We compare this method.
 - Controlroom3dSchult et al. [2024]: controlroom3d generate indoor scene based on custom layout. And it did not open source.
 - DreamSceneLi et al. [2024a]: DreamScene introduces Formation Pattern Sampling (FPS) to balance semantic information and shape consistency, and a three-stage camera sampling strategy to improve the quality of scene generation. Dreamscene require predefined 3D layouts as input and only receives relative positional information of objects. We create the relative positional json file according to layout. We compare this method.
 - SceneCraftYang et al. [2024a]: SceneCraft trains a 2D diffusion model conditioned on bounding box image and employ a SDS loss for optimization. It also require pre-defined layouts and camera trajectory. we use nerfstudio to create the same layout for training. And we custom the camera trajectory. We compare this method.
- Object Retrieval Framework: not only pre-trained diffusion model, but a large database of furniture. Therefore, if comparison is needed, we only compare the layout generation.
 - AnyhomeFu et al. [2024]: the first object retrieval framework that utilize LLM to generate multi-room scene. AnyHome is not fully open-source; we compare the layout generation with anyhome.
 - * AnyHome filters out some improperly placed objects, resulting in large blank areas.
 - InstructSceneLin and Mu [2024]: InstructScene trains a diffusion model to generate layout for single room generation. We compare the layout generation with InstructScene.
 - * Only tackle single room.
 - * Diversity in the generated layouts is reduced due to the limited size of the training dataset.

- ArchitectWang et al. [2024b]: Architect first apply a diffusion model to inpaint an empty scene, then pre-trained depth estimation models to lift the generated 2D image to 3D space. We compare the large furniture layout generation.
 - * The masked area is usually located in the center, causing the model to tend to generate objects in the center of the room, with almost no objects along the walls.
 - * There is no strict constraint on the spatial relationships between bounding boxes, allowing for potential overlaps between different bounding boxes.
- Holodeck Yang et al. [2024b]: holodeck leverages a large language model for common sense knowledge about what the scene might look like and uses a large collection of 3D assets from Objaverse to populate the scene with diverse objects.
 - * Holodeck tends to position objects along walls, resulting in less varied layouts.

7.3.2 Object Generation

- Consistent3DWu et al. [2024b]: Consistent3d explores the ODE deterministic sampling prior for 3D generation. However, Consistent3d leverage nerfMildenhall et al. [2021] as 3D representation that ray tracing methods can not incorporate into our framework. Additionally, Consistent3d is a two stage method and our method is one step. Hence, we did not compare this methods.
- CFDYan et al. [2025]: CFD and Consistent3D initialize 3D model by MVDreamShi et al., and Our model initializes by point-eNichol et al. [2022]. we did not compare this methods.
- CCDLi et al. [2024b]: CCD shares the same insight as the Consistent3dWu et al. [2024b] and also incorporate consistency modelSong et al. [2023]. We compare this methods.
- LuciddreamerLiang et al. [2024]: Variants of the SDS loss.
- DreamLCMZhong et al. [2024]: A sds loss that use the latent diffusion model as based model. However, it did not open source.
- VividdreamerChen et al. [2024b]: A sds loss that use the latent diffusion model as based model. We compare this methods.
- DreamSceneLi et al. [2024a]: We also compare with it.

7.3.3 Environment Optimization

Although some worksChen et al. [2024a], Huang et al. [2024b], Wang et al. [2024a] address the generation of both environmental and furniture textures, our approach is limited to layout textures for planar surfaces only. Consequently, we conduct ablation studies to validate the effectiveness of our approach.

7.4 Explanation of Experiments

We explain the comparison results in Figure 5 of regular paper.

As shown in Figure 17 and Figure 18, Set-the-scene is nerf-composition methods that struggles with generalization across objects of varying scales and suffers from overexposure issues; text2roomHöllein et al. [2023] fails to generate surfaces in regions outside the camera views; DreamSceneLi et al. [2024a] lacks geometric priors of the environment, causing the environment and furniture to merge during optimization, resulting in artifacts and multi-view inconsistencies; SceneCraftYang et al. [2024a] fine-tunes a 2D diffusion model for scene generation tasks; however, its inherent inability to model multi-object synergies leads to significant generation deficiencies in complex layout scenarios, resulting in incomplete structured scene outputs.

- DreamSceneLi et al. [2024a]: **DreamScene’s floorplan is automatically generated, creating the smallest possible enclosure that contains all objects. This is why DreamScene’s layout differs from ours.**
- SceneCraftYang et al. [2024a]: Our layout’s scale differs from SceneCraft’s, making direct replication impossible. We manually adapt our layouts (via NeRFStudio) to match SceneCraft’s format. As shown in Figure 19.
- However, despite we create the compatible layout for SceneCraft, it still generates unsatisfied results.



Figure 17: Comparisons of SceneLCM and baselines.



Figure 18: Comparisons of SceneLCM and baselines.

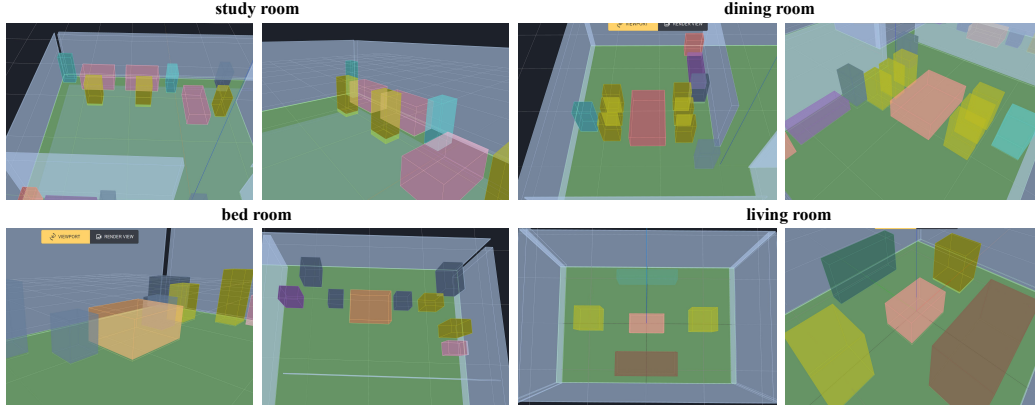


Figure 19: Layout of SceneCraft.

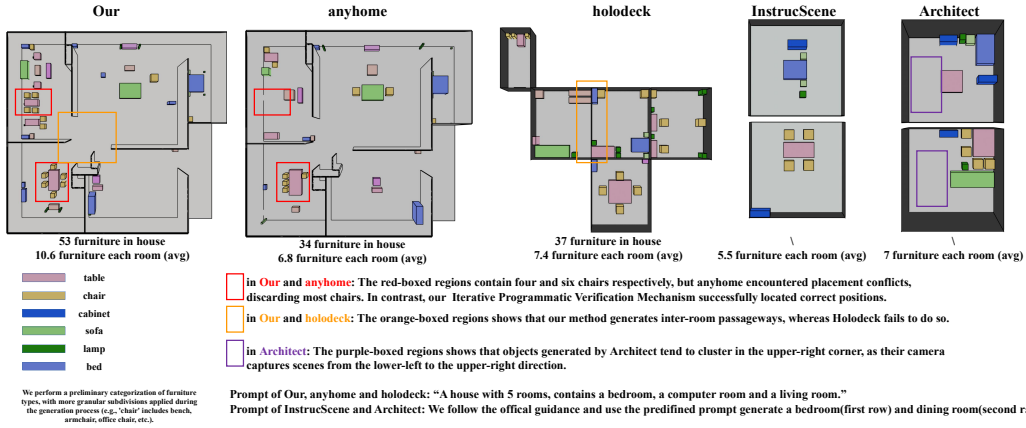


Figure 20: Layout Comparison with 4 baseline. AnyHomeFu et al. [2024] generates unreasonable layouts due to partial furniture omission. HolodeckYang et al. [2024b] fails to create inter-room passageways and tends to align objects along walls. InstructSceneLin and Mu [2024] and ArchitectWang et al. [2024b] are limited to single-room generation with simplistic layouts.

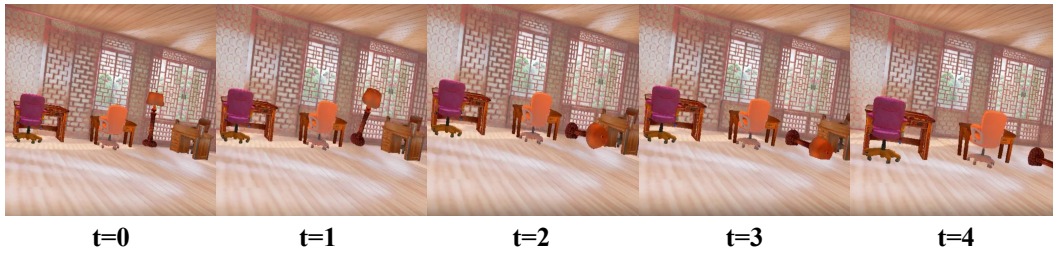


Figure 21: physical editing. Tilting the room by 30 degrees causes objects to slide downward due to gravity.



Figure 22: objects results

7.5 Additional Experiments

- We conduct comparative experiments on layout generation.
- We conduct additional experiments on 2 house layout which contain 4 rooms and 3 rooms respectively. We conducted experiments across 4 houses, comprising a total of 16 rooms and over 182 furniture items. As shown in Figure 24, 25, 26, 27.
- We provide additional visual results for both environments and objects.
- Physically plausible editing for multi-objects. As shown in Figure 21, our model adheres to physical laws during the editing process.
- Editing

7.5.1 Comparative Experiments on Layout

To ensure fairness, all comparison models are using GPT-4. We use the same floorplan generative model as anyhomeFu et al. [2024]. Therefore, we first generate the floorplan, and then our method and AnyHome generate layouts on the same floorplan respectively. holodeckYang et al. [2024b], ArchitectWang et al. [2024b] and InstructSceneLin and Mu [2024] generate a json file for saving bounding box of objects, we directly plot these bounding box in blenderCommunity [2018]. Additionally, InstructScene did not generate walls, which were manually created by us.

As shown in Figure 20, our methods can generate more furniture and ensure the reasonable layout.

7.5.2 More Results on House Generation

We provide the video in our file. Due to time constraints, we cannot present the results here. The demonstration video has been included in the supplementary materials.

7.5.3 Visual Results on Environment and Furniture

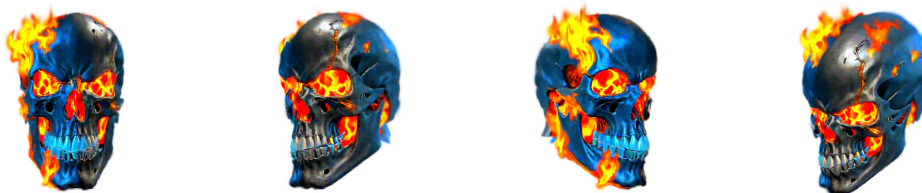
We provide the video in our file. Furniture results as shown in Figure 22. We also provide some other results in Figure 23.



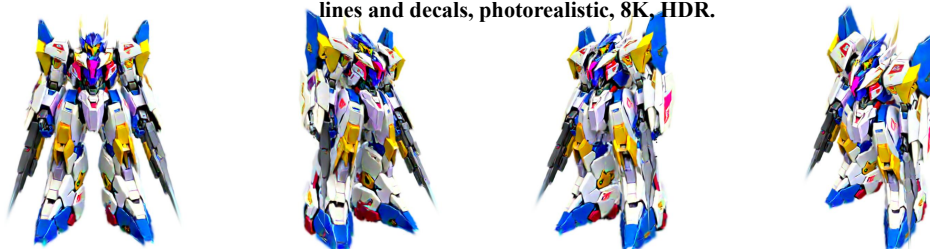
A portrait of Groot, head, HDR, photorealistic, 8K



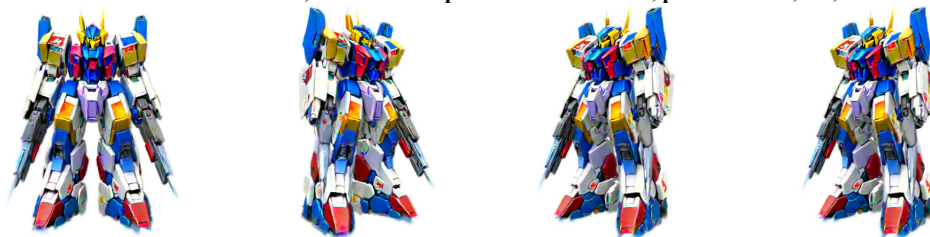
A portrait of batman, head, photorealistic, 8K, HDR.



A portrait of the Ghost Rider, head, HDR, photorealistic, 8K.



A Gundam Barbatos Lupus Rex model, Gundam, Barbatos, with detailed panel lines and decals, photorealistic, 8K, HDR.



A Gundam model, with detailed panel lines and decals, photorealistic, 8K, HDR.

Figure 23: object results

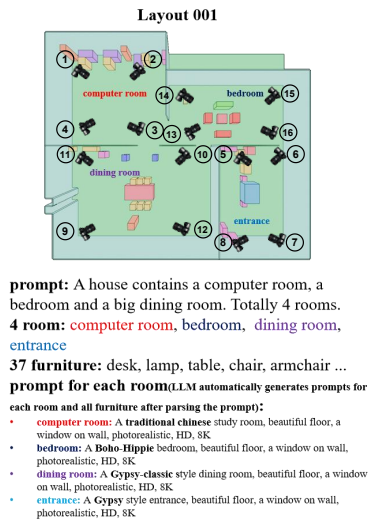


Figure 24: Additional Experiments Results for layout 1.

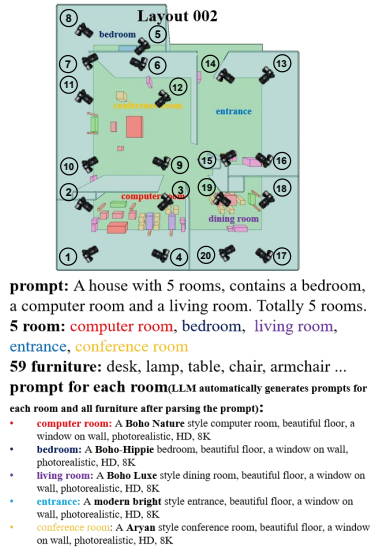


Figure 25: Additional Experiments Results for layout 2.

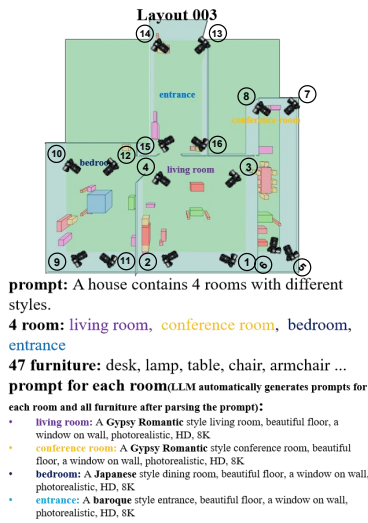


Figure 26: Additional Experiments Results for layout 3.

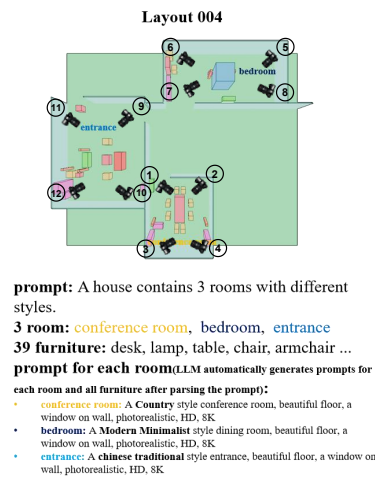


Figure 27: Additional Experiments Results for layout 4.

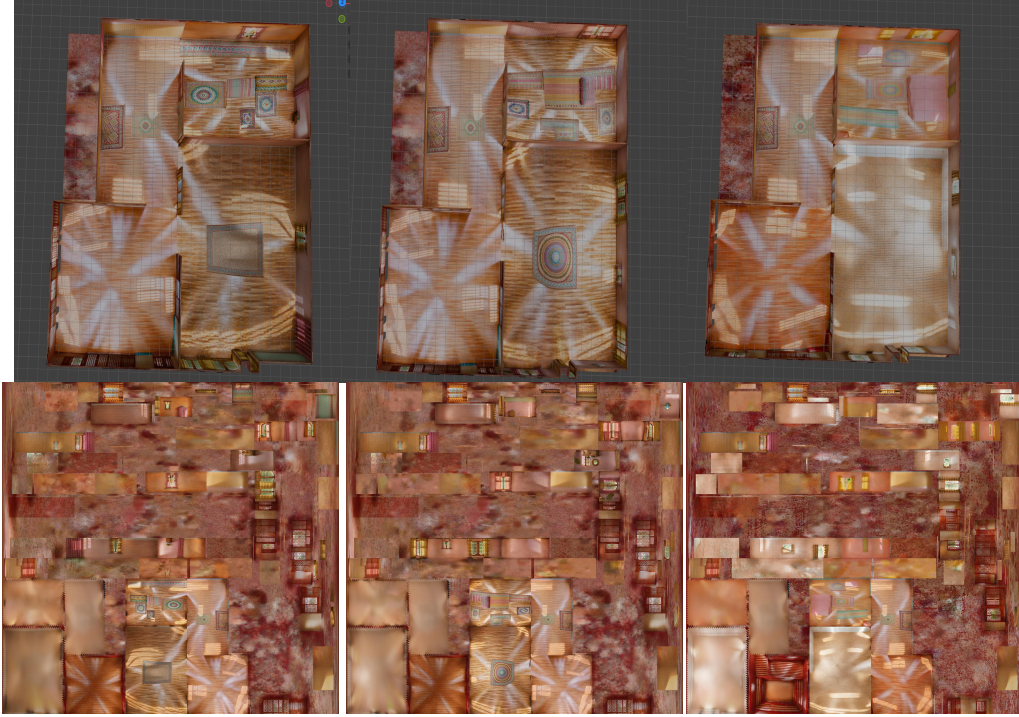


Figure 28: Environment Editing. We can export the texture map and editing the texture via texture map.

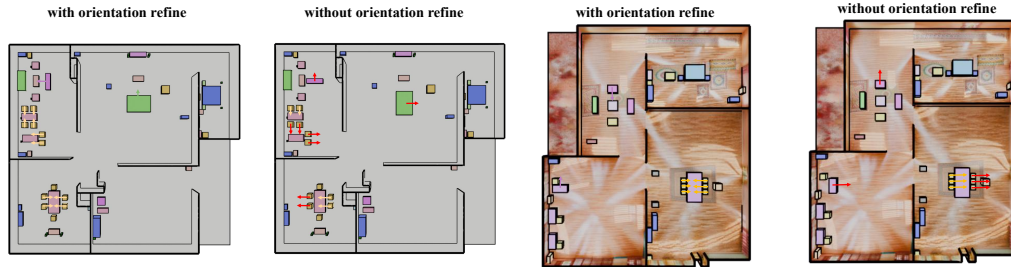


Figure 29: Ablation Study of Cluster-based Orientation Assignment. Red arrows indicate incorrect object orientations, as LLMs tend to generate uniform orientations for identical objects. Our method effectively corrects these inaccurate orientations.

7.5.4 Editing

- Environment Texture Editing: As shown in Figure 28.
- Furniture Editing:
 - Create
 - Delete
 - Remove
 - Update

7.6 Ablation Study

7.6.1 layout generation

- Interactive Programmatic Verification Mechanism: As shown in Figure 20, without our proposed method, we would encounter the same issue as anyhomeFu et al. [2024], where partial furniture is discarded, resulting in blank areas within the generated layouts.



Figure 30: Ablation Study of noise removal.

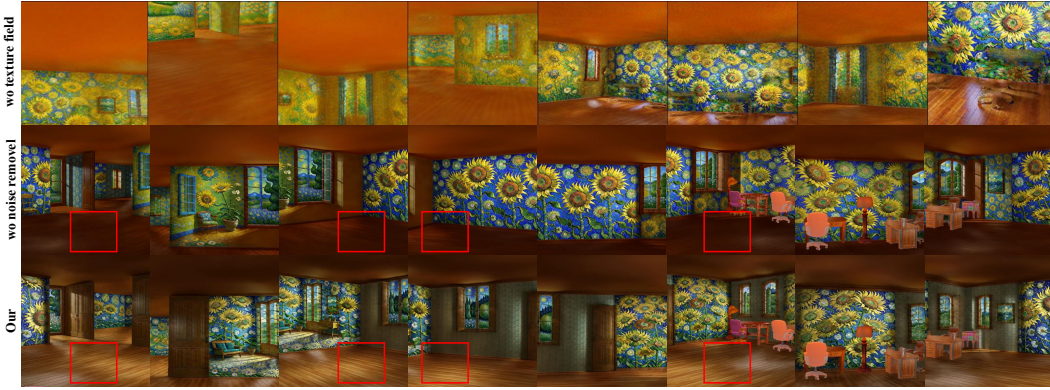


Figure 31: Ablation Study of noise removal and texture field on scene level(prompt: "A room in the style of Van Gogh"). Noise removal not only enhances the realism of generated scenes but also facilitates the generation of finer details, such as floor textures and patterns. Texture fields enable the generation of more intricate and detailed representations, while employing a unified neural network for UV coordinates significantly enhances spatial consistency. The first four images in Row 1 (left) and the subsequent four images (right) depict the same scene from different perspectives, revealing inconsistent floor styles.

- Cluster-based Orientation Assignment Strategy: As shown in Figure 29, some inaccuracy orientation can be fixed after Orientation Assignment Strategy.

7.6.2 object generation

We conduct an ablation study of noise removal, as shown in Figure 30. Noise removal has texture with more detail and faster generation. To achieve comparable performance, adding noise requires 4,000 rounds (36 minutes), while denoising necessitates 3,000 rounds (28 minutes).

7.6.3 environment optimization

- Multi-resolution texture field: As shown in Figure 31.
- Noise Removal: As shown in Figure 31.
- normal-aware decoder: As shown in Figure 32, normal-aware decoder can generate much more details.



Figure 32: Ablation Study of normal decoder. Obviously, normal-aware decoder can generate much more details.



Figure 33: Ablation Study of camera trajectory. Placing the camera at the center results in the inability to capture combined entities (wall + floor + ceiling), preventing the model from recognizing the current entity's semantics and causing texture blurriness.

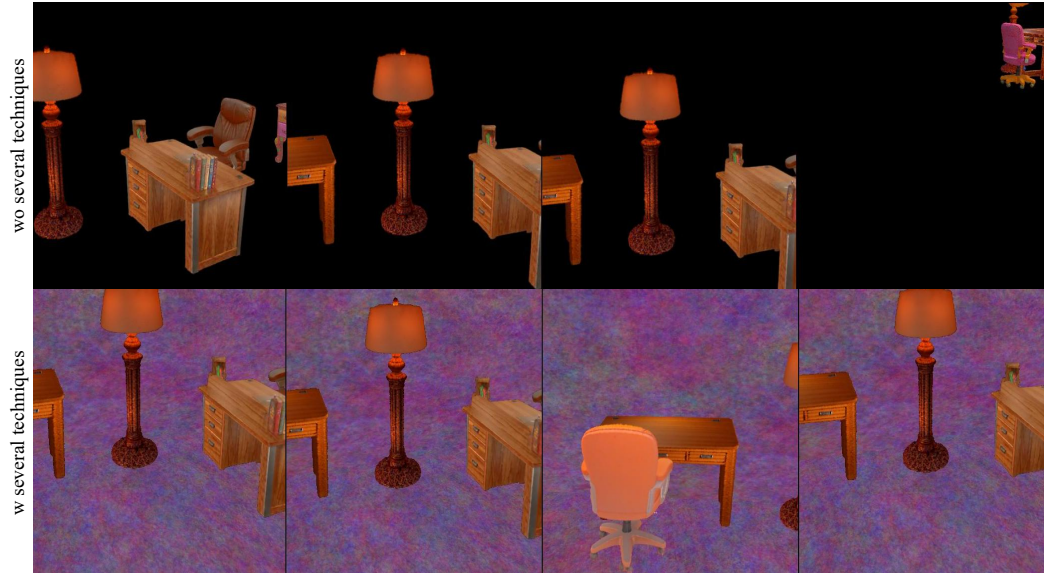


Figure 34: Ablation Study of several techniques. These techniques introduce additional randomness into our initialization process, enabling successful optimization. Note: Final results are not presented here, as our model cannot converge without these techniques.

- zigzag camera trajectory: we use the sphere camera trajectoryChen et al. [2024a], Li et al. [2024a] for comparison, as shown in Figure 33. Additionally, we conduct extensive experiments on rooms of diverse scales to validate the robustness of our method.
- several techniques: these techniques are prepared for numerical stability. As shown in Figure 34.